UNIVERSITY OF OSLO
Department of Physics

Polar cap patch occurrence rate over Svalbard and it's dependence on IMF By

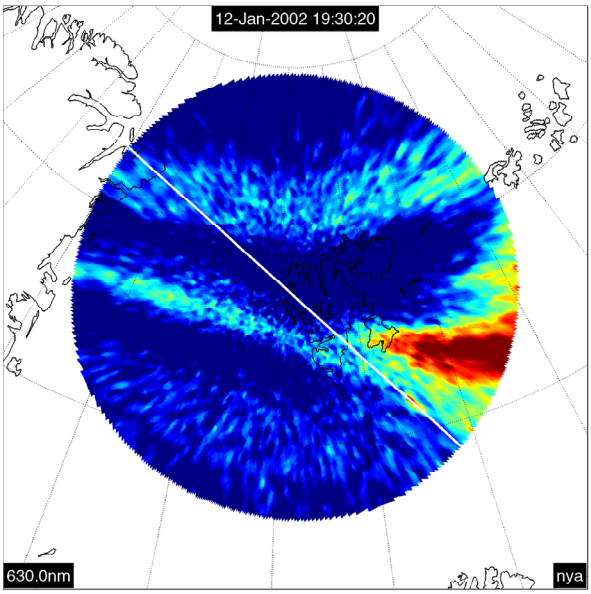

Master Thesis

Njål Gulbrandsen

December 2006

UNIS

UNIVERSITAS OSLOENSIS
MDCCCXI

Abstract

Polar cap patches are regions of enhanced plasma density, seen to drift from the sunlit ionosphere on the day side, over the polar cap, and into the night side Auroral oval. The patches are related to substorm activity and reconnection processes in Earth's magnetic tail.

The fact that the patches crosses the open-closed field line boundary (OCB) and goes into the poleward edge of the aurora, can be used as an indicator of the night side merging gap, and the ongoing reconnection processes in the tail.

A statistics of the occurrence of polar cap patch OCB crossings at the night side and its dependence on IMF By are made using data from Meridian scanning photometer (MSP) and All-sky camera (ASI) in Ny- Ålesund, Svalbard. This statistics can give indications of the positioning of the night side merging gap and it's IMF By dependence.

Polar cap patches was found to cross the night side OCB over Svalbard in the interval 18:30 – 04:50 MLT with an average of 23:25 MLT, more than half an our before magnetic midnight. The changes in IMF B_y seems to be able to move the area where patches crosses the OCB by $\sim$ 1 hour MLT.

Acknowledgments

I would like to thank the following people for their contributions to this thesis:

- Todd Pedersen from the American Air Force Research Laboratory (AFRL) for providing all-sky images from the AFRL camera in Ny-Ålesund.
- Gabrielle Provan from University of Leichester for help with making the SuperDARN convection plots.
- Espen Trondsen and Bjørn Lybekk from University in Oslo for providing data, software and technical assistance.
- ACE SWEPAM and MAG instrument teams and the ACE Science Center for providing the ACE data.
- My supervisors Jøran Moen and Dag Lorentzen for letting me do parts of this work at the University center in Svalbard (UNIS).
- And everyone else who has been of help, especially these last months.

Contents

Chapter 1

Introduction

Polar cap patches are regions of enhanced plasma density, seen to drift from the sunlit ionosphere on the dayside, over the polar cap, and into the night side Auroral oval. The patches are related to substorm activity and reconnection processes in Earth's magnetic tail.

The fact that the patches crosses the open-closed field line boundary (OCB) and goes into the poleward edge of the aurora, can be used as an indicator of the night side merging gap, and the ongoing reconnection processes in the tail.

In this study we want to make a statistics of the occurrence of polar cap patch OCB crossings at the night side by using data from Meridian scanning photometer (MSP). This statistics can then give an indication of the positioning and extent of the night side merging gap.

We also want to check this statistic for any dependence on the interplanetary magnetic field (IMF). We know that the convection pattern in the ionosphere is highly dependent upon the IMF conditions, and that the patches are going to follow this convection. We would therefor expect a slightly shift in the patch occurrence times.

To be able to interpret the MSP data it is sometimes useful to compare them to all-sky images to see "the bigger picture" and what really is going on. We have therefor chosen to take one of our days of MSP data and compare with all-sky images. We where also lucky to get some all-sky images from American Air Force Research Laboratory (AFRL) who operates a very sensitive all-sky camera in Ny-Ålesund. We therefor took the opportunity to compare data from this camera to the images from the UiO camera.

This study has also been a process of improving the ways we process optical data. Some new techniques has been tried and some old routines has been improved. Hopefully some of these tecniques will prove usefull for others.

Chapter 2

Background

2.1 Plasma

A plasma is simply ionized gasses where electrical and magnetically interactions dominates. Plasma is fairly common on our universe and exist everywhere where gasses have a sufficiently high temperate or low pressure or both. The sun and the stars consist of plasma, and a large amount of the material in between planets and especially the solar wind consist of plasma.

2.1.1 Single particle motion

If we assume no collisions or other interactions between particles a plasma can be described by single particle motions. These can be derived from the equation of motion for charged particles:

$$m\frac{\mathrm{d}\mathbf{v}}{\mathrm{d}t} = q(E + \mathbf{v} \times \mathbf{B}) \tag{2.1}$$

Where m is the particle mass, q is the particle charge and E and B is electric and magnetic field respectively. If we assume an homogeneous magnetic field B and that there is no electric field E the solution to equation (2.1) gives a circular motion around a magnet field line with a gyrating frequency Ω_c and gyro radius r_c.

$$\Omega_c = \frac{qB}{m} \qquad r_c = \frac{mv_\perp}{qB} \tag{2.2}$$

The motion along the magnetic field is not affected by the magnetic field and the particle will therefor continue with unchanged velocity in the direction parallel to the magnetic field. If we include a electric field E perpendicular to the magnetic field, the solution would give us a motion that is a combination of this gyrating motion and a constant motion perpendicular to both E and B called $\mathbf{E} \times \mathbf{B}$-drift. This constant motion can be derived by averaging over one gyro period. This particle drift velocity is given as:

$$v_c = \frac{\mathbf{E} \times \mathbf{B}}{B^2} \tag{2.3}$$

This motion does not give rise to any currents while electrons and protons will drift in the same direction with the same drift speed. This gives us an important relation between drift velocity and electric field.

Actually any extra force upon the charged particles will generate a drift motion:

$$v_f = \frac{\mathbf{F} \times \mathbf{B}}{qB^2} \tag{2.4}$$

This could give rise to currents if the force is charge independent.

A magnetic field line is usually a wage quantity in physics. When we in space physics use the therm "magnetic field line" we most often mean the gyro center of the particles. So when a field line is moving it is actually the guiding centers of the particles that are moving. (Kivelson and Russel, 1995; Pécseli, 2005).

2.1.2 Magneto Hydro Dynamics (MHD)

Magneto Hydro Dynamics is a fluid-model used to describe plasma. It is derived combining Maxwell's' equations with fluid dynamics and Ohm's law (Pécseli, 2005):

Divergence less **B**

$$\nabla \cdot \mathbf{B} = 0 \tag{2.5}$$

Faraday's induction law

$$\nabla \times \mathbf{E} = -\frac{\partial \mathbf{B}}{\partial t} \tag{2.6}$$

Ampère-Maxwell's law

$$\nabla \times \mathbf{B} = \mu_0 \mathbf{j} \quad \left(+ \mu_0 \varepsilon_0 \frac{\partial \mathbf{E}}{\partial t} \right) \tag{2.7}$$

Ohm's law

$$\mathbf{j} = \sigma(\mathbf{E} + \mathbf{v} \times \mathbf{B}) \tag{2.8}$$

Continuity equation

$$\frac{\partial \rho}{\partial t} + \nabla \cdot (\rho \cdot \mathbf{v}) = 0 \tag{2.9}$$

Navier-Stokes equation

$$\rho \frac{\mathrm{d}\mathbf{v}}{\mathrm{d}t} = -\nabla p + \rho \mathbf{g} + \mathbf{j} \times \mathbf{B} \tag{2.10}$$

In addition an equation of state is needed to close the set of equations. The simplest is to assume incompressibility:

$$\nabla \cdot \mathbf{v} = 0 \tag{2.11}$$

This will for a lot of cases give satisfying results. It is also possible to assume that the process is adiabatic giving the following equation of state:

$$p = \text{const} \cdot \rho^{\gamma} \qquad \gamma = \frac{C_p}{C_v} \tag{2.12}$$

2.1.3 Frozen-in-field

Using the equations in section 2.1.2 we can demonstrate a useful property with plasma. Taking equation (2.8) we get

$$\mathbf{E} + \mathbf{v} \times \mathbf{B} = \frac{\mathbf{j}}{\sigma} \tag{2.13}$$

inserting it in (2.6) gives

$$\frac{\partial \mathbf{B}}{\partial t} = -\nabla \times \left(\frac{\mathbf{j}}{\sigma} - \mathbf{v} \times \mathbf{B} \right) \tag{2.14}$$

Using (2.7) and neglecting the displacement current

$$\mathbf{j} = \frac{1}{\mu_0} \nabla \times \mathbf{B} \tag{2.15}$$

which combined with (2.14) gives

$$\frac{\partial \mathbf{B}}{\partial t} = -\frac{1}{\mu_0 \sigma} \nabla \times (\nabla \times \mathbf{B}) + \nabla \times (\mathbf{v} \times \mathbf{B}) \tag{2.16}$$

Using the vector relationship

$$\nabla \times (\nabla \times \mathbf{B}) = \nabla(\nabla \cdot \mathbf{B}) - \nabla^2 \mathbf{B} \tag{2.17}$$

in combination with (2.5) gives

$$\frac{\partial \mathbf{B}}{\partial t} = \frac{1}{\mu_0 \sigma} \nabla^2 \mathbf{B} + \nabla \times (\mathbf{v} \times \mathbf{B}) \tag{2.18}$$

where the first term is a diffusion term and the second term is an convection term. As long as the conductivity σ is high, the velocity v isn't to small and the length scale we are locking at isn't to small. The convection term will dominate over the diffusion term. This is expressed in the Magnetic Reynolds' number:

$$R_m = LV \mu_0 \sigma \tag{2.19}$$

where L is characteristic length and V is characteristic velocity. As long as $R_m \gg 1$ the diffusion term is negligible and we get the equation:

$$\frac{\partial \mathbf{B}}{\partial t} = \nabla \times (\mathbf{v} \times \mathbf{B}) \tag{2.20}$$

One implication of equation (2.20) is the so called "frozen-in-field" meaning that the plasma is locked to the magnetic field and has to move with it. This is important for our study since we then can assume that every plasma movement is a movement of the magnetic field and every movement of magnetic field is a movement of plasma.

2.2 Magnetosphere, IMF and Magnetic reconnection

Earth's magnetic field can often be considered as an dipole field in the near space around earth. This would also be the case far away from earth if it hadn't been for the solar wind. The solar wind consist of ionized particles (plasma) coming from the sun carrying with it it's own magnetic field. When the solar wind interacts with the earth's magnetic field it gets compressed at the day side and stretched at the night side as seen in figure (2.1).

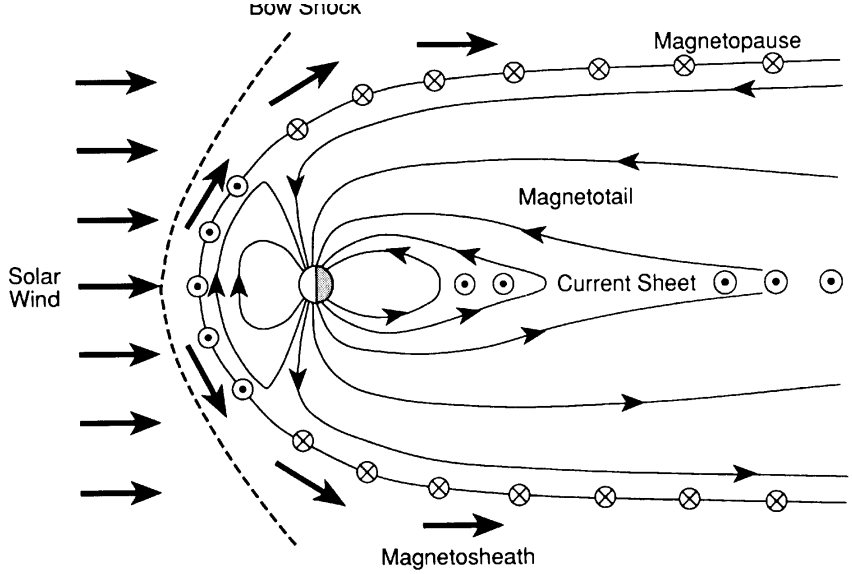

Figure 2.1: The earth's magnetosphere with a compressed day side and a stretched night side. At the magnetopause and in the current sheet in the tail there are currents going due to shear in the magnetic field. The solar wind is deflected by bow shock upstream from the magnetopause. (Kivelson and Russel, 1995).

The border region between earth's magnetic field and the solar wind is called the magnetopause and consist of an current carrying layer of plasma. The region inside the magnetopause where earth's magnetic field is dominating is called the magnetosphere. According to Ampère-Maxwell's law (equation 2.7) any share (or curl) in a magnetic field must give rise to a current. In the magnetosphere we call such areas current sheets and we find them at the magnetopause where solar wind hits the magnetosphere and in the middle of magnetotail were magnetic fields of opposite direction meet (figure 2.1).

2.2.1 Magnetic reconnection

In some areas in the current sheets magnetic field of opposite direction gets compressed in a small area the "frozen-in-field" condition (section 2.1.3) breaks down and we get a diffusion of magnetic field lines according to equation (2.18). The magnetic field lines reconnects in an other configuration , as seen in figure (2.2). In this new configuration the curvature of the field lines creates a tension force acting away from the diffusion region as it tries to straiten out the field line. This force then accelerate particles in the current sheet away from the diffusion region as seen in figure (2.2). Reconnection is sometimes also called magnetic merging.(Paschmann, 1991; Kivelson and Russel, 1995)

2.2.2 Convection

Dungey (1961) suggested a model where under periods with IMF B_z negative there would be two such sites with reconnection. One at the front side magnetopause and one in the magnetotail (see figure 2.3). These two reconnection sites drives a cycle that leads to a transport of magnetic flux antisunward across the polar cap with a return flow at the dawn and dusk sides (figure 2.3).

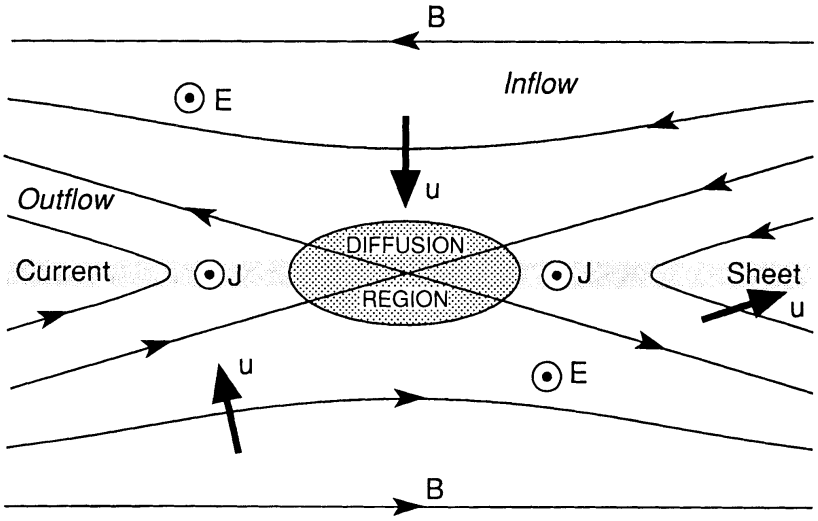

Figure 2.2: Schematic drawing of magnetic reconnection. (Kivelson and Russel, 1995)

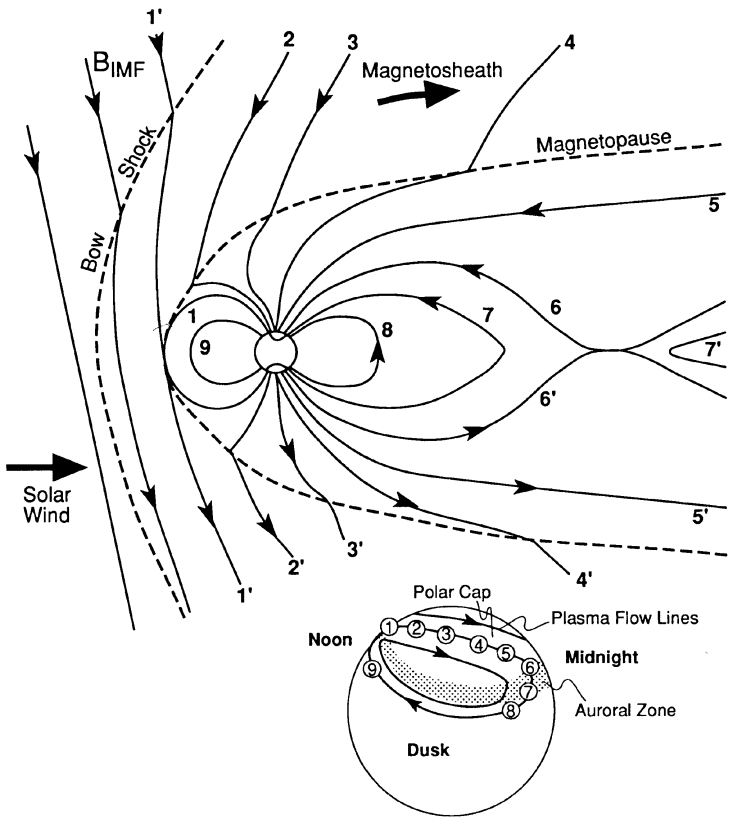

Figure 2.3: Illustration of the Dungey cycle. The number sequence follows a magnetic field line from it reconnects at the magnetopause (1) and drift over the polar cap and reconnects again in the tail (6) and then return to the front side (9). The lower image shows how this cycle is seen in the ionosphere.(Kivelson and Russel, 1995).

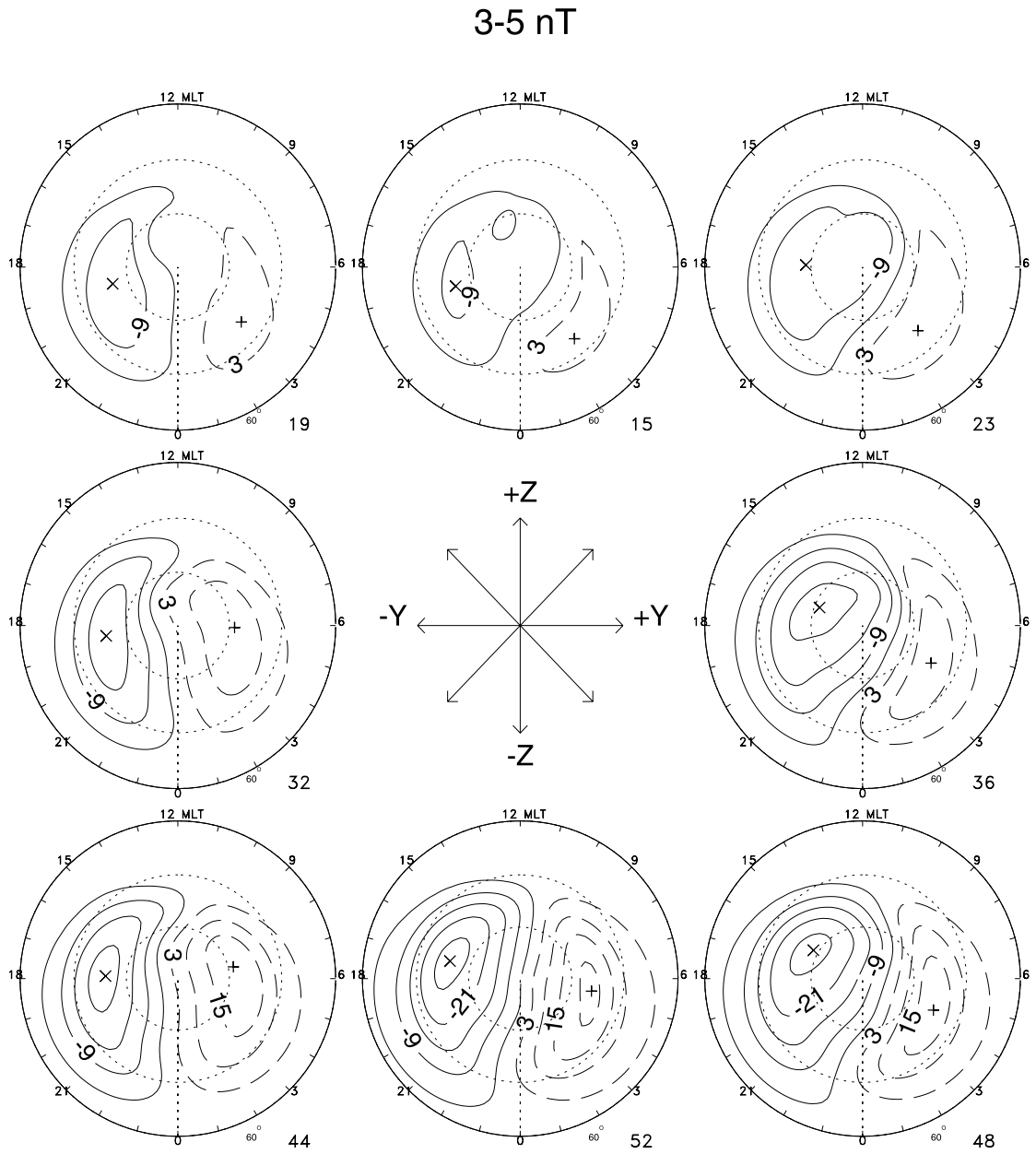

Figure 2.4: Statistical convection patterns sorted by clock angle in the GSM Y-Z plane for the 3–5 nT interval of IMF magnitude.(From Ruohoniemi and Greenwald, 2005)

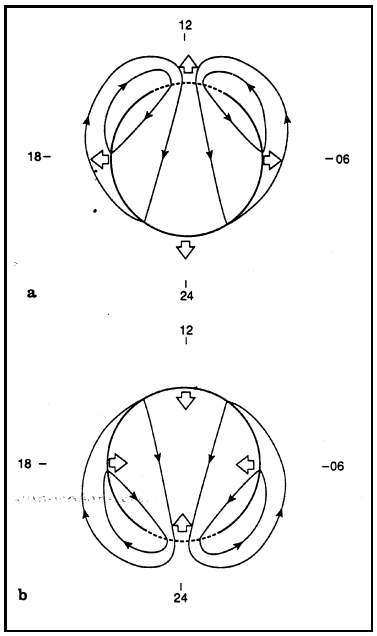

Figure 2.5: The two components of the reconnection driven convection patterns in the ionosphere. The circle is the open-closed field line boundary and the dashed line is the merging gap mapping to active reconnection site. (a) shows the effect of day side reconnection bringing more open flux into the polar cap making the OCB expand southwards. (b) shows the night side reconnection taking closing open flux and making polar cap area with open flus shrink. (Cowley and Lockwood, 1992).

Cowley and Lockwood (1992) discuss the growth and decay of this convection related to IMF. They use the expansion and contraction of the polar cap area of open flux as an explanation for the flow. The area where flux enters or exits the polar cap, called the merging gap, maps to areas with active reconnection (figure 2.5). This is the only places flux can enter or exit the polar cap. All other places the OCB has to follow the plasma flow. The day side reconnection and thereby the day side flux transfer to the polar cap is controlled by the IMF B_z while a dominating B_y component will introduce an asymmetry between the convection cells (Cowley, 1981).

Several statistical studies of the response of the convection pattern has been made in later years (Weimer, 1995; Ruohoniemi and Greenwald, 1996, 2005). Figure (2.4) shows a plot from such a study by Ruohoniemi and Greenwald (2005) made with the SuperDarn radar network. As can be seen form the figure the convetion pattern isn't symetric even when the IMF is strictly B_y-negative.

2.3 Ionosphere

The ionosphere is a region in the atmosphere from 50 km to 500 km that is electricly conductive due to ionisation by solar radiation. It is devided into several layers acording to diferent peaks in the electron density profile (figure 2.6). The typical height of ionospherical layers are given in table (2.1).

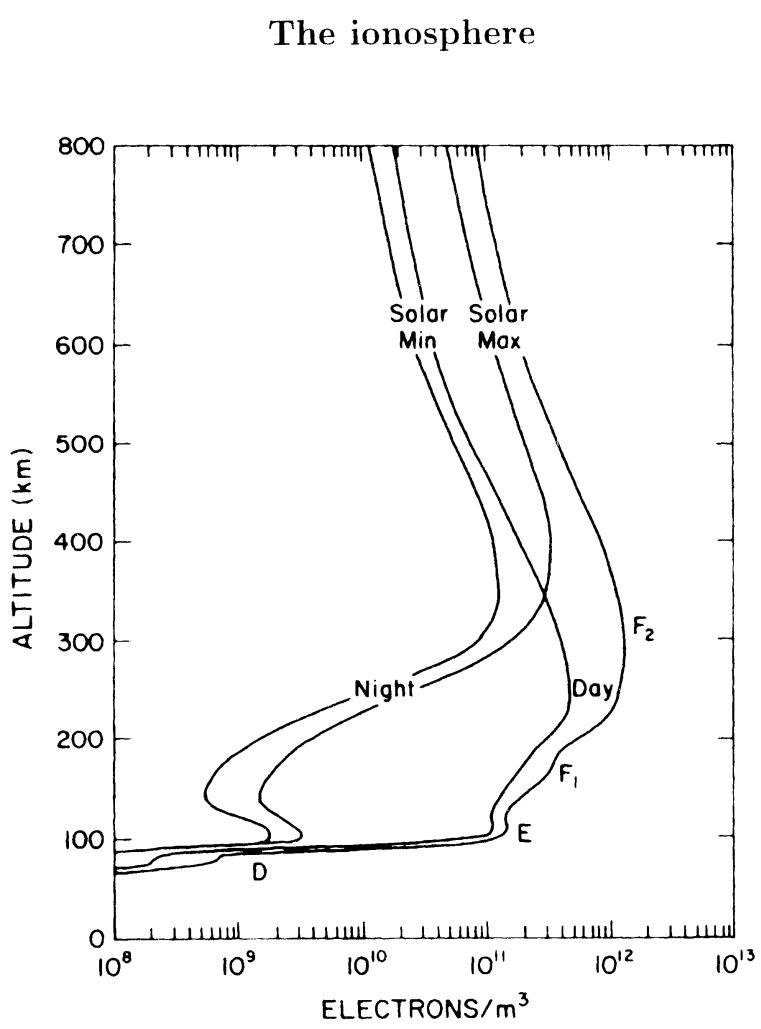

Figure 2.6: Typical electron profiles for the ionosphere.(Brekke, 1997)

layer	height [km]
F-layer	150 – 500
E-layer	95 – 150
D-layer	50 – 90

Table 2.1: Layers in the ionosphere.

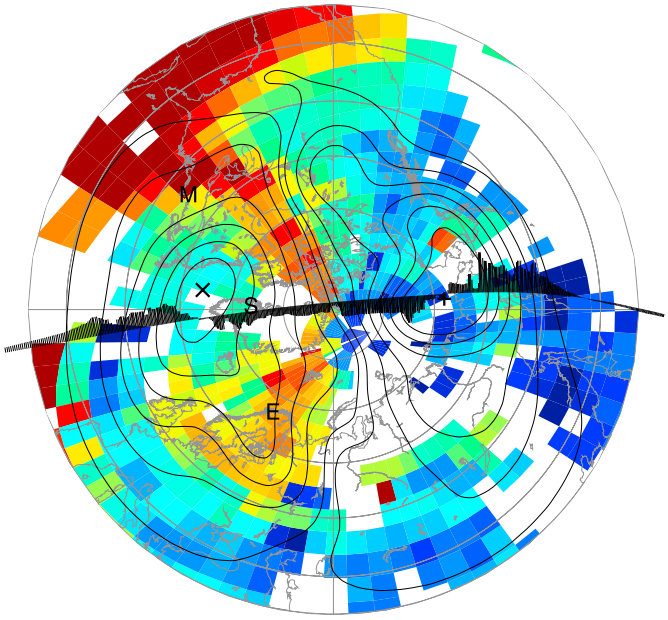

Figure 2.7: Polar projection of the TEC plume. The TOI is seen to extend continuously from its low-latitude source in the prenoon sector, through the dayside merging gap and across the polar cap to the midnight sector. (From Foster et al., 2005)

2.4 Polar cap patches

Polar cap patches are electron-density enhancements in the ionospheric F region. The formation mechanism for patches are still not fully understood (Sojka et al., 1993, 1994; Carlson, 1994; Rodger et al., 1994), but it is widely believed that patches are solar ionized plasma that has been transported through the daytime merging gap with the ionospheric convection in form of a tongue-of-ionization (TOI). Figure (2.7) shows a total electron content (TEC) map where a tongue-of-ionization is seen to stretch from the low latitudes at the day side, through the convection throat and over to the night side.

Polar cap patches are found in horizontal scales from 100 – 1000 km (Crowley, 1996) and Lorentzen et al. (2004) measured their height to be around 300 km.

Polar cap patches are visible as airglow at 630.0 nm due to recombination of atomic oxygen. Crowley (1996) mentions possible optical definition of a patch. The first is has to be 50 R above the 630.0 nm background intensity. The second is it has to be more than 50% above the 630.0 nm background.

Polar cap patches are mainly present in when IMF B_z is negative. When IMF B_z is positive the polar cap is dominated by polar arcs (Carlson, 1994). Figure 2.8 shows a schematically drawing of the two states of the polar ionosphere. Coley and Heelis (1998) found that the IMF B_y dependence of the flow direction for polar cap patches is consistent with the B_y dependency of the general antisunward convection.

Lorentzen et al. (2004) managed to link patch OCB crossings with substorm activity. When a patch gets sucked into the nighttime aurora it has to have crossed the open-closed field line boundary (OCB), and the only place to cross is through the merging gap. A plasma flow through the nighttime merging gap has to be due to a reconnection (see Cowley and Lockwood, 1992). Lorentzen et al. (2004) therefor suggested using polar cap patch OCB crossings as indication of ongoing tail reconnection.

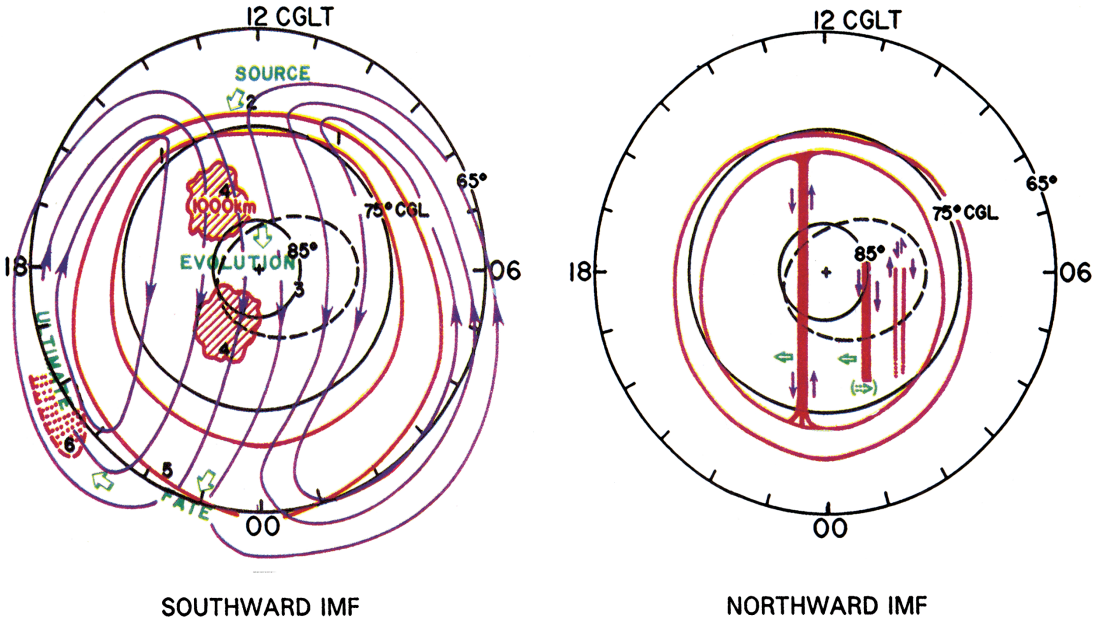

Figure 2.8: The two states of the polar ionosphere. Polar cap patches are dominating when the IMF is southwards while polar arcs are more common when IMF is northwards. Optical emission is drawn in red. (Carlson, 1994)

2.5 Coordinate systems

2.5.1 GSM

All IMF data in this thesis is given in GSM coordinates (Geocentric Solar Magnetoshereic System). This coordinate system is centered i the center of Earth. The x-axis is pointing from earth to the sun. The y-axis is perpendicular to earth's magnetic dipole putting the dipole axis in the x-z plane. The positive z-direction then lies in the northern hemisphere (Kivelson and Russel, 1995).

The clockangle is the angle between the z-axis and the projection of the IMF vector in the y-z plane in the GSM coordinate system. The clockangle can be calculated using the following equations:

$$\theta = \arctan\left(\frac{B_y}{B_z}\right) \tag{2.21}$$

for $B_z > 0$, and

$$\theta = 180^\circ + \arctan\left(\frac{B_y}{B_z}\right) \tag{2.22}$$

for $B_z < 0$

2.5.2 Geomagnetic coordinates and Magnetic local time

Since most of the processes going on in the ionosphere are governed by earth's magnetic field it is often useful to coordinate system that relates a point to the magnetic field. The simplest way to achieve this is to make a system where the magnetic dipole axis is the z-axis instead of earth's rotational axis. To convert from geographic latitude (λ) and longitude (ϕ) to magnetic latitude (λ_m) and longitude (ϕ_m) the following equations are used (Brekke, 1997):

$$\sin\lambda_m = \sin\lambda_p \sin\lambda + \cos\lambda_p \cos\lambda \cos(\phi - \phi_p) \tag{2.23}$$

$$\sin\phi_m = \frac{\cos\lambda}{\cos\lambda_m} \sin(\phi - \phi_p) \tag{2.24}$$

The magnetic dipole declination ψ can then be calculated as:

$$\sin\psi = -\frac{\cos\lambda_p}{\cos\lambda_m} \sin(\phi - \phi_p) \tag{2.25}$$

And the magnetic local time (MLT) can be calculated:

$$t_{MLT} = t_{UT} + \frac{\Psi}{15^\circ} \tag{2.26}$$

The magnetic local time is the time given with the suns position relative to the magnetic pole. Magnetic midnight is then when sun is at the opposite magnetic meridian as the observing site. The auroral oval is thought to follow MLT.

Using the geographic position of the magnetic pole in a dipole approximating from 2005, $\lambda_p = 79.3^\circ$ and $\phi_p = 288.2^\circ$, we have calculated geomagnetic position an magnetic local time for some sites (table 2.2). Our observation site, Ny-Ålesund, has from this model a magnetic midnight at 20:50 UT.

location	latitude [°]	longitude [°]	mag. lat.[°]	mag. lon. [°]	MLT corr. [h]	MLT midnight
Pole (2005)	79.3	288.2	90.0	0	0	24:00
Ny-Ålesund	78.90	11.90	75.50	49.85	-3.1658	20:50
Longyearbyen	78.20	15.83	74.45	49.67	-2.92	21:05
Tromsø	69.66	18.94	67.00	62.82	-1.8913	22:06
Oslo	59.93	10.75	59.59	78.96	-1.4220	22:35

Table 2.2: Geomagnetic coordinates and magnetic local time

2.5.3 Corrected Geomagnetic coordinates (CGM) and AACGM

Corrected Geomagnetic coordinates (CGM) is a coordinate system that in addition to convert latitude and longitude also account for the magnetic field differences by height. This is done by tracing a position with the International Geomagnetic reference field (IGRF). One problem with CGM is that there is an area around equator where it is undefined. This problem is solved width the Altitude Adjusted Corrected Geomagnetic coordinates(AACGM), a version of CGM that uses a spherical harmonics expansion of coordinate transformation (Baker and Wing, 1989). The AACGM coordinates are, among other, used by the SuperDARN system (Ruohoniemi and Baker, 1998).

Since the location of the magnetic poles are slowly changing. The magnetic midnight of an observation site changes with time as well. In figure (2.3) we have listed the magnetic midnight calculated using AACGM for some years included in this study.

year	MLT midnight [UT]
1999	20:49
2000	20:50
2001	20:51
2002	20:52
2003	20:53
2004	20:54
2005	20:55

Table 2.3: Magnetic midnight for 300 km above Ny-Ålesund calculated using AACGM (Calculated at NASA/Goddard Space Flight Center, ModelWeb).

Chapter 3

Instrumentation

3.1 All-sky cameras

An all-sky camera (ASC) or an all-sky imager (ASI) is a camera system made to monitor the whole sky at once. This is usually accomplished by using a fish-eye lens as front optics, but there exist system that uses convex mirrors as well. Ideally should an all-sky camera have a field-of-view of 180°.

3.1.1 UiO All-Sky Camera in Ny-Ålesund

The UiO All-Sky Camera in Ny-Ålesund is an intensified monochromatic All-Sky Camera produced by Keo Consultants, Brookline, MA, USA (now Keo Scientific Ltd.). The system consist of: Front optics, a filter wheel, a re imaging system, an image intensifier and a CCD camera (KEO Consultants, 1995). As front optics it uses a 3-inch Mamiya 24mm f/4 fisheye lens (KEO Consultants, 1993). The image intensifier is an air cooled 25 mm Gen II (Enhanced blue cathode). The CCD camera is a Photometrics Series CH200 back illuminated monochromatic CCD with 512 × 512 pixels and 12-bit intensity resolution. It has three narrow band interference filters. For routine observation a 630.0 nm filter and a 557.7 nm filter is used. In addition it also has a 427.8 nm filter. The bandwith of all of the filters are 2nm. The filter wheel is temperature controlled to keep the filter stable at these wavelengths. The camera is set up to take two red (630.0 nm) and four green (557.7 nm) pictures a minute with an exposure time of 1 – 2 s for

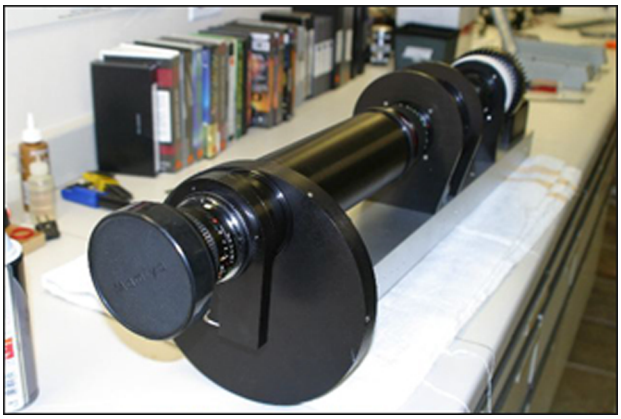

Figure 3.1: An all-sky camera similar to the one in Ny-Ålesund (KEO Scientific Ltd.)

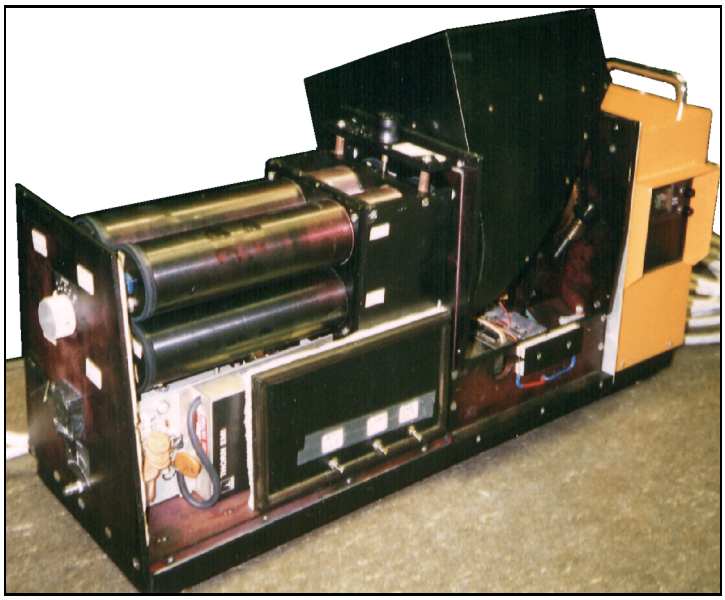

Figure 3.2: The Meridian Scanning Photometer in Ny-Ålesund. The photomultiplier tubes are seen to the left, and to the right of them is a black box containing the movable mirror.

630.0 nm and 0.5 – 1.5 s for 557.7 nm.

3.1.2 AFRL All-Sky Camera in Ny-Ålesund

In addition to the UiO all-sky camera we have also used some images from the camera the American Air Force Research Laboratory (AFRL) operates in Ny-Ålesund. This camera works in the same way as the one owned by UiO, but it uses a 4-inch front lens making it more light sensitive, and thereby have less noise in the images. It also uses a 670 × 650 pixel CCD. We have only used 630.0 nm filtered data from this camera.

3.2 Meridian Scanning Photometer (MSP)

The Meridian Scanning Photometer measures intensities along the magnetic north-south. This is accomplished by having a movable mirror scanning 160°in front of a set of photomultiplier tubes. The recordings are done simultaneously in four channels, 630.0 nm, 557.7 nm, 427.8 nm and 486.1 nm

3.3 ACE

The satellite ACE – Advanced Composition Explorer, was launched by NASA in 1997. It is located in an orbit around the first Lagrange point (L1) of the Sun-Earth system ∼240 R_E sunward of Earth (see fig. 3.3). A Lagrange point is a stable point in a gravitational three body system. The satellite is spinning with 5 rpm and the rotational axis is pointing toward the Sun.

The ACE satellite carries nine scientific instruments (Stone et al., 1998), but only data from the MAG and SWEPAM instruments are being used in this thesis.

The Magnetic Field Experiment (MAG) uses two triaxial flux-gate magnetometers mounted on booms extending 4.19 meters from the center of the spacecraft. It measures the magnetic

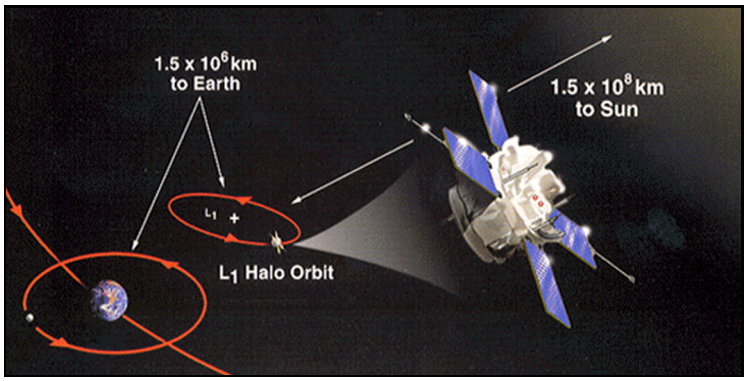

Figure 3.3: The ACE satellite and the location of it's orbit around the first Lagrange point (ACE mission website)

field in the solar wind in three dimensions in the satellites reference system, which later is converted to a geocentered coordinate system. The system has a sampling rate of 24 vector samples/s which could be stored in a snapshot memory or it can use 3,4, or 6 vector samples/s in continuous data stream (Smith et al., 1998).

Solar Wind Electron, Proton, and Alpha Monitor (SWEPAM) measure electrons and ions energy and fluxes in the solar wind. From these measurements parameters as solar wind velocity and particle densities are derived. The system use separate sensors for ions and electrons. The ion sensor measure energies between 0.26 and 36 KeV and the electron sensor measures energies between 1 and 1350 eV. The instrument has a time resolution of 64 s (McComas et al., 1998).

The data used for this study is 64 seconds averages of level 2 data for both the MAG and the SWEPAM measurements. The level 2 quality is data where the instrument teams has applied calibration and detector response maps (Garrard et al., 1998).

3.4 SuperDARN

SuperDarn – the Super Dual Auroral Radar Network is a network of coherent-scatter HF radars. The network consist of 9 radars in the northern hemisphere and 6 radars in the southern hemisphere. The radars measure velocities of the large scale polar cap convection in the ionospheric F region. A single radar can only measure velocities along the line-of-sight. By having radars with overlapping field-of-view two dimensional velocity vectors can be derived. To get usable information also outside these common field-of-views the measurement together with data from a statistical convection model (Ruohoniemi and Greenwald, 1996) are used to determine a spherical harmonics expansion of electrostatic potential (Ruohoniemi and Baker, 1998). In the ionospheric F region electrostatic potential isolines can be considered as flow lines for the plasma convection due to the $\mathbf{E} \times \mathbf{B}$ drift .

Chapter 4

Methods

4.1 All Sky cameras

4.1.1 Noise reduction/filtering of all-sky images

The intensity of polar cap patches is very weak (∼100 – 1000 R) compared to the aurora. It is also in the lower range of what the UiO all-sky camera can detect, and that puts it in the same intensity range as the noise from the image intensifier. There might also be other processes leading to this noise like clouds or small scale structures in the air glow. But since we in this study are interested in large scale structures it might be useful to remove this noise to be able to see the large scale structures better. This can be obtained by using different types of image filtering. I've chosen to use a median filter since this is one of the most efficient filters when it comes to noise reduction.

A median filter is a filter that generates the pixels in the filtered image by taking the median value of the pixel values in a box surrounding the same pixel position in the original image (See fig. 4.1). One problem with this filter is that there is no obvious way to calculate the pixels at the edges since they can not be surrounded by a box without the box getting outside the image. The solution chosen here is just to skip the edges in the filtered image making it a bit smaller than the original.

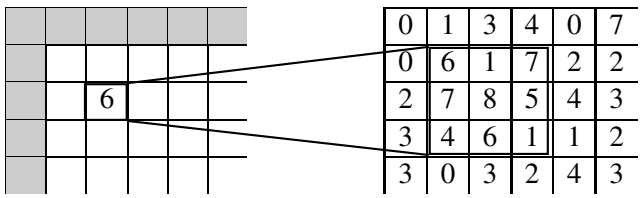

Figure 4.1: An example of an 3×3 median filter. A pixel in the filtered image is generated by taking the median value of a 3×3 box surrounding the same pixel position in the original image.

One advantage with a median filter is that it doesn't introduce any pixel values that doesn't exist in the original image. It also is a so called edge preserving filter in that if you have a sharp edge of a structure that is larger than half the size of the filter box, this edge would be preserved as it is, while if you for example used a mean filter (same type but use mean instead of median), it will smoothen out the edge of any structure.

For the all-sky images a 5×5 median filter was used. It works basically in the same way as the filter described in figure 4.1, but uses a 5×5 pixel box instead of an 3×3 pixel box. Figure

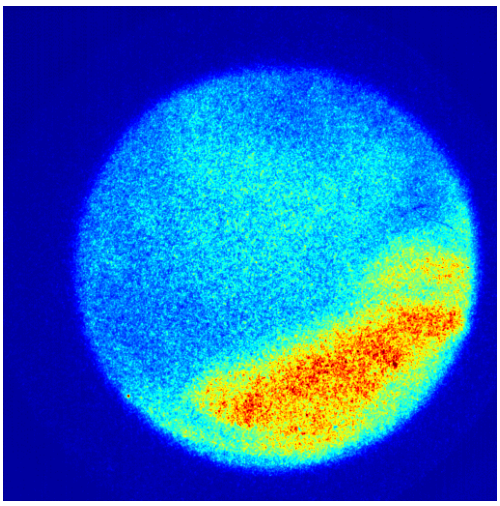

(a) Raw CCD image plotted on a linear falsecolored scale

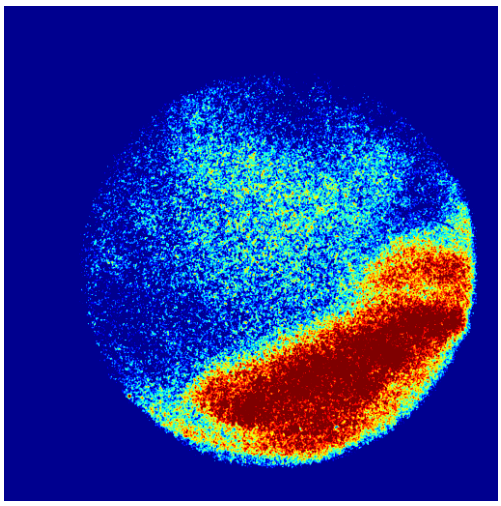

(b) Same image as in (a) plotted in a logarithmic scale

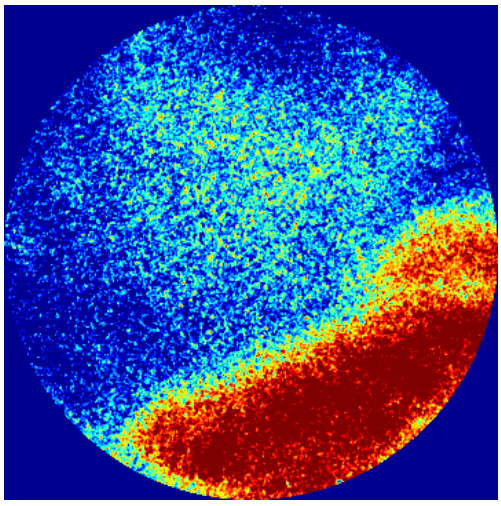

(c) The image (b) centered and cropped to 140° field-of-view

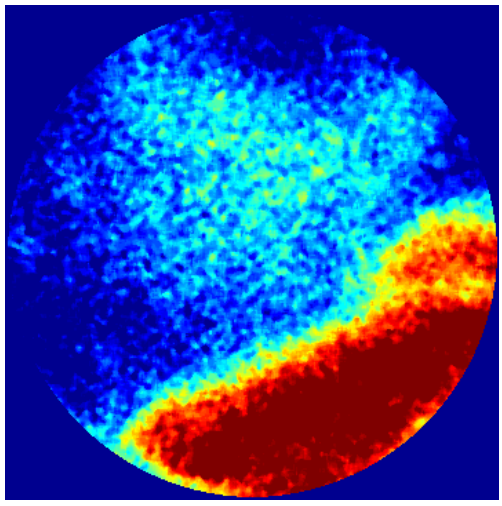

(d) The image (c) after applying a 5×5 median filter

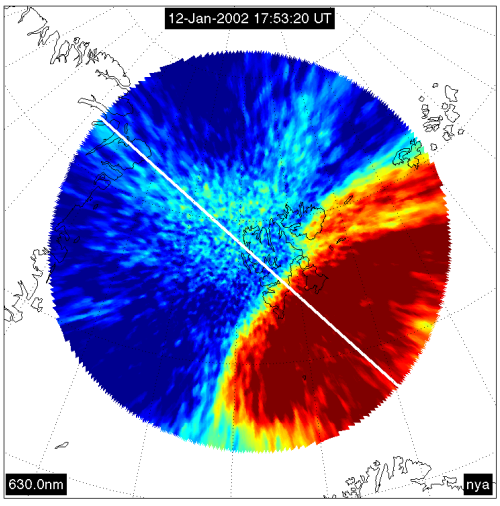

(e) The image (d) projected assuming plane paralell atmosphere. The white line crossing the image represent the MSP scan line.

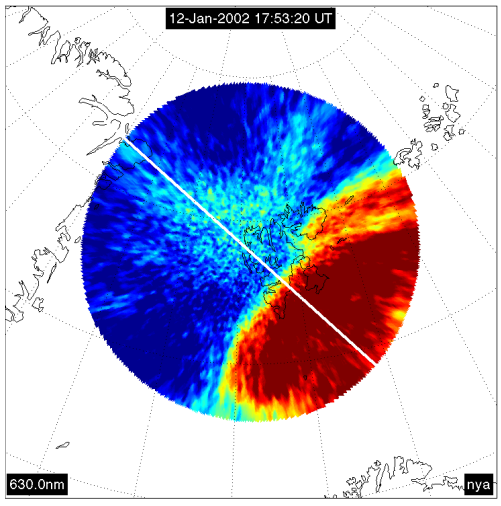

(f) The image (d) projected assuming curved atmosphere. The white line crossing the image represent the MSP scan line.

Figure 4.2: The process from a raw CCD image to a map projection. The images are plotted in a false colour scale to make it easier to see the different intensity regions.

4.2c and 4.2d shows a all-sky image before and after median filtering.

One disadvantage with median filters is that the operation of taking the median uses a lot of processor time.

4.1.2 Projection of All-Sky images

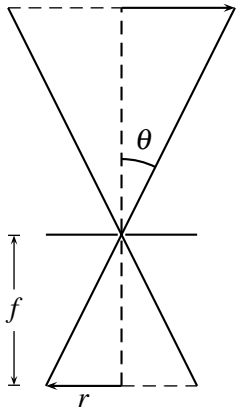

Figure 4.3: Schematic drawing of a pin-hole camera. f is the focal length, θ is the angle of the incident ray and r is the distance from the center of the image

A fish-eye-lens, like the ones used as front optics for all-sky cameras, gives a large distortion of the image compared to ordinary lenses. This is because it is not possible to image a 180° field-of-view onto a plane with ordinary optic (KEO Consultants, 1993). Ordinary optics should ideally work the same way as a pinhole camera where all the light goes through a single point and is imaged on to a plane, as shown in figure (4.3). Then the image is just a magnification or demagnification of the object. This is also called Gnomical projection, and is expressed by:

$$r = f\tan(\theta) \tag{4.1}$$

where r is the distance from center in the image, f is the focal length and θ is the angle of the incident ray.

Gnomical (pinhole)	$r = f\tan(\theta)$
Equidistant (linear)	$r = f \cdot \theta$
Orthographic	$r = f\sin(\theta)$
Equisolid angle (Equal area)	$r = 2f\sin\left(\frac{\theta}{2}\right)$
Stereographic	$r = 2f\tan\left(\frac{\theta}{2}\right)$

Table 4.1: Different projections used in fish-eye lens design. (KEO Consultants, 1993)

The all-sky cameras used in this thesis have projections that are close to equidistant projection. That means that the distance from the center in the image is proportional to the incident angle

$$r = f \cdot \theta \tag{4.2}$$

where θ is given in radians.

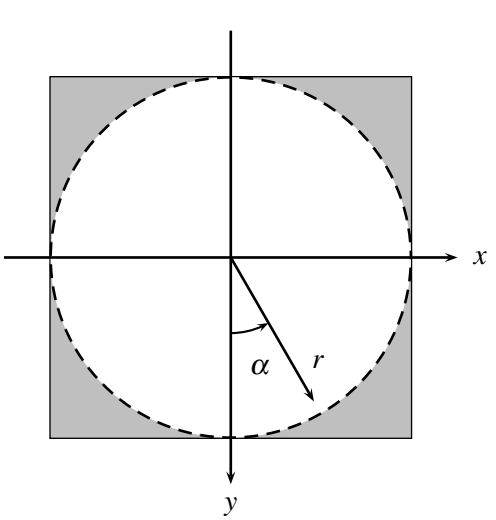

(a) The coordinate system used to organize the CCD data. The y-axis is pointing downward because the sky is seen from underneath with an all-sky camera, while the map projection is "seen from above"

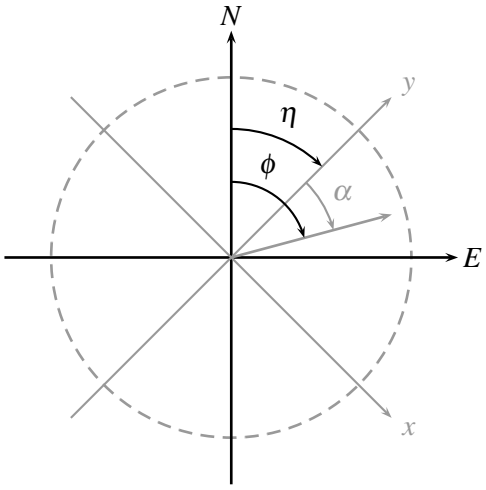

(b) The geographical coordinate system. (The transformed CCD coordinate system shown in gray)

Figure 4.4: The horizontal coordinate system transformation from the CCD to geographical coordinates

Before an image is projected on to a map we need to find the center of the all-sky image. It is also useful to crop the image to a certain field-of-view since everything imaged from an angle of 90° from zenith (Horizontally) should be projected on to infinity. Here we have chosen to crop the image at 70° (140° field-of-view). The image before centering and cropping can be seen in figure (4.2a) and (4.2b), while figure (4.2c) shows how it is after cropping.

To be able to project the image we have to make a coordinate system with origin in the center of the image. We take

$$x = (p_x - p_{x,0}) \qquad y = -(p_y - p_{y,0}) \tag{4.3}$$

Where (p_x, p_y) is the pixel coordinate in the image file and $(p_{x,0}, p_{y,0})$ is the pixel coordinate of the center. The use of minus in front of the y coordinate might depend upone the coding of the image data and what program is used to read the data. The resulting coordinate system can be seen in figure (4.4a). Since we know that the outer border of the image should correspond to 70°we can use equation (4.2) and the relation $r = \sqrt{x^2 + y^2}$ to calculate a focal length for the system.

$$f = \frac{r}{\theta} = \frac{r_{max}}{\theta_{max}} \tag{4.4}$$

An incident angle is then calculated for every pixel in the image using equation (4.2) and (4.4).

$$\theta = \frac{r}{f} = \sqrt{x^2 + y^2} \cdot \frac{\theta_{max}}{r_{max}} \tag{4.5}$$

The angle α in figure (4.4a) can be calculated using:

$$\alpha = \arctan\left(\frac{x}{y}\right) \tag{4.6}$$

for $x > 0$, and

$$\alpha = 180^\circ + \arctan\left(\frac{x}{y}\right) \tag{4.7}$$

for $x < 0$.

To convert this angle to the geographical coordinate system we need to know the direction of the y-axis relative to geographic north. This angle has been measured when the camera was set up, so we can then easy calculate the direction relative to north.

$$\phi = \alpha + \eta \qquad \eta : \text{Camera's angle relative geographic north} \tag{4.8}$$

It is also worth to note that the geographical direction ϕ is consider positive turning clockwise from north (see figure 4.4b).

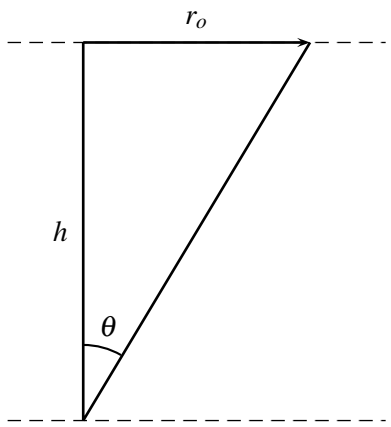

Figure 4.5: Hight projection in a plane parallel atmosphere

To be able to calculate a geographical position for every pixel we need to project the image to a certain height. The simplest way to do this is to assume a plane parallel atmosphere as shown in figure 4.5. The horizontal distance r_o from the center can then be calculated using

$$r_o = h\tan(\theta) \tag{4.9}$$

Knowing the coordinates of the instrument site, the horizontal distance and the direction, the geographical latitude and longitude could be calculated using the MatLab Mapping Toolbox.

4.1.3 Correction for the curvature of Earth

To assume a plane parallel atmosphere is a bit inaccurate when it comes to the distances used here. We might have to correct for the curvature of Earth.

From figure 4.6 we find the following relations:

$$(R_E + h)\cos\Theta = R_E + s\cos\theta \tag{4.10}$$

$$(R_E + h)\sin\Theta = s\sin\theta \tag{4.11}$$

From (4.11) we get

$$s = (R_E + h)\frac{\sin\Theta}{\sin\theta} \tag{4.12}$$

and inserted into (4.10) it gives us

$$(R_E + h)\cos\Theta = R_E + (R_E + h)\frac{\sin\Theta}{\sin\theta}\cos\theta \tag{4.13}$$

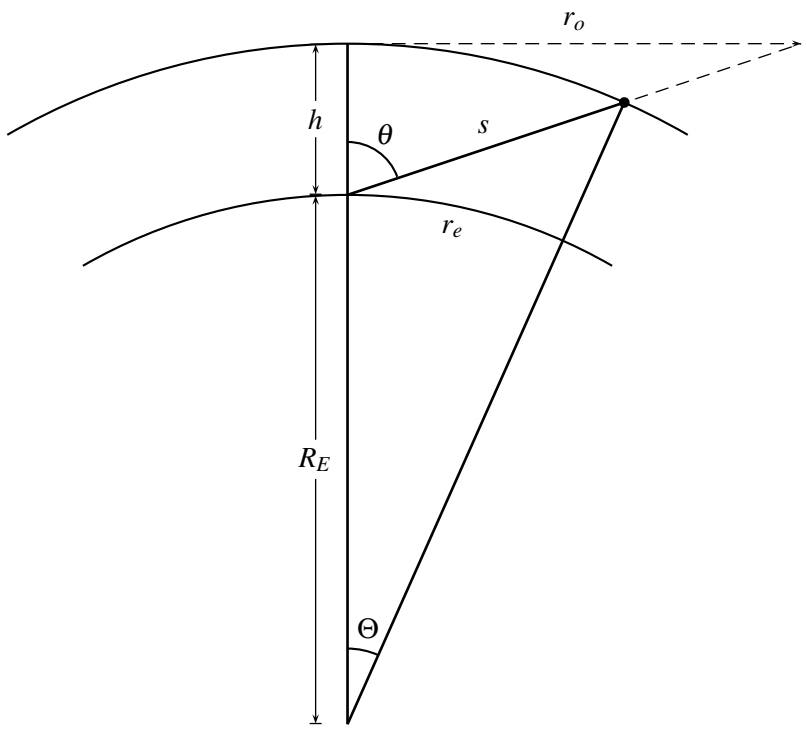

Figure 4.6: Schematic drawing of how to do hight projection in a curved atmosphere. The r_o is the distance calculated using a plan parallel atmosphere while r_e is the distance calculated using curved atmosphere

$$\cos\Theta - \sin\Theta\frac{\cos\theta}{\sin\theta} = \frac{R_E}{R_E+h} \tag{4.14}$$

which then can be written

$$\sin\theta\cos\Theta - \cos\theta\sin\Theta = \frac{R_E}{R_E+h}\sin\theta \tag{4.15}$$

Using the trigonometric relations

$$\sin(\theta-\Theta) = \sin\theta\cos\Theta - \cos\theta\sin\Theta$$

gives

$$\sin(\theta-\Theta) = \frac{R_E}{R_E+h}\sin\theta \tag{4.16}$$

$$\Theta = \theta - \arcsin\left(\frac{R_E\sin\theta}{R_E+h}\right) \tag{4.17}$$

The distance at Earth's surface can then be calculated

$$r_e = R_E\cdot\Theta = R_E\left[\theta - \arcsin\left(\frac{R_E\sin\theta}{R_E+h}\right)\right] \tag{4.18}$$

Where Θ is given in radians. Using the equation (4.18) with an angle of 70°, $R_E = 6.37\cdot10^6$ m and a projection height $h = 300$ km gives a distance for r_e of 686.9 km. The same calculations using (4.9) gives a distance for r_e of 824.2 km. This shows that the curvature of Earth is significant at these distances. In figure (4.7) the projection distanse is plotted as a function of incident angle for both atmosphere models.

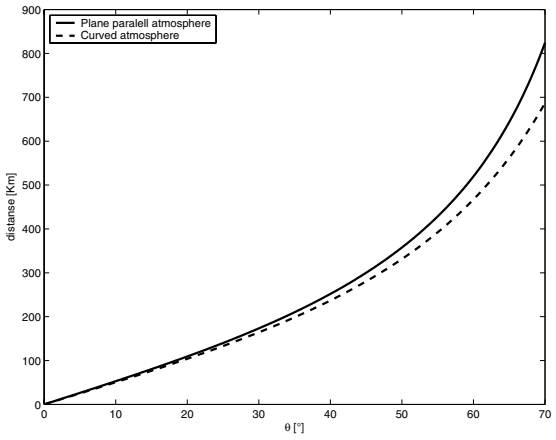

Figure 4.7: A comparison between flat and curved atmosphere.

4.1.4 Flat-field correction

Unfortunately the sensitivity of an all-sky camera has a certain dependence on the angle of the incident ray. The sensitivity is largest at zenith and decrease toward the edges of the image. Ideally this should be solved by making a full scale calibration for all angles so that the intensities could be given in Rayleights. When this is not possible there exist other methods to flatten the radiation field. The method described here actually has the advantage that it could be done a long time after the measurements has been taken. Actually you only need the measurements itself.

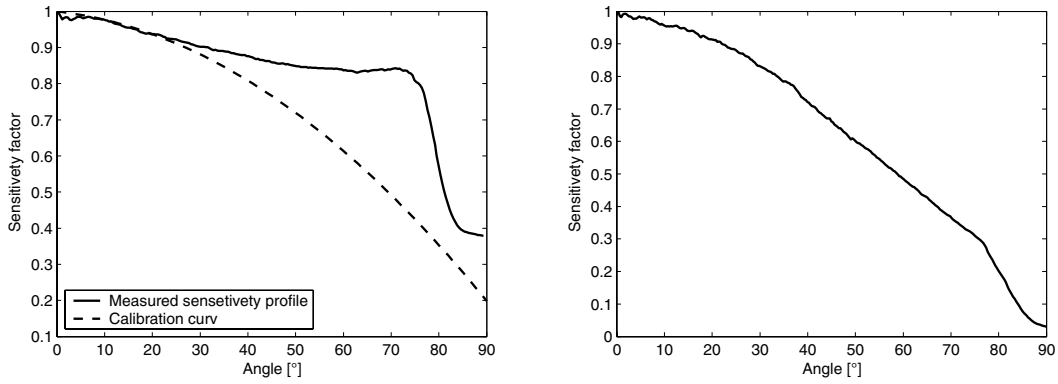

(a) UiO (b) AFRL

Figure 4.8: Measured intensity profile and constructed flat-field for the UiO and the AFRL all-sky camera. (a) The solide line is the derrived profile for the UiO camera, while the dashed line is the calibration profile for the same camera. (b) The derrived profile for the AFRL camera.

The important thing is to find a period of the data where the sky is more or less evenly lit, at least in average. Then you add together all the images in that period hoping that the small variations in the images would even out over time. It's of course important that the time period isn't to short. We used a period of two hours from 22:00 UT until 24:00 UT from 12. January 2002 (Se chapter 5). For this period of time only some weak patches where drifting over the camera. They were drifting trough the whole field-of-view of the camera, and should therefore in average give a uniform lighting in the two hour period. The image we then got was divided

by it's maximum value so that the resulting image had values between 1 and 0. If this image then looks nice and symmetric it could be used as it is. When an image then later would be divided by this flat-field image the result will be an image corrected for this sensitivity variation. But there is a possibility to process the data further. If the flat-field image is a bit uneven we can try to find a average or typical angular dependence.

What we did was to get a radial profile for direction ($0^\circ - 360^\circ$) with 1° resolution. These profiles could then be averaged together or even better, as we have done, take the median of them. This will ensure that any sudden intensity spikes in the data is left out. This radial profile will then give the dependence on incident angle, and can be used to create a new flat-field image with no azimuth angle dependence. This procedure was done for both cameras and the profiles are shown in figure (4.8). For the UiO camera we also had a calibration done in year 2000. The calibration profile is given by a 2. order fit to the calibration data:

$$S(\theta) = \frac{\left(-8.23 \cdot 10^{-5}\theta^2 - 1.5 \cdot 10.^{-3}\theta + 1\right)}{8.618 \cdot 10^3} \cdot E \tag{4.19}$$

Where E is the exposure time given in ms. A scaled version of this calibration profile is plotted in figure (4.8a) for comparison. As seen in figure (4.8a) the measured sensitivety factor from the data deviates a lot from the calibration profile, espesialy at larger angles. This difference might be due to atmospheric conditions. We are locking at radiation from atmosperic constitunse located at a certain height. If we assume this to be a uniform layer of radiation, a large zenith angle means that the radiation comes from a larger volum of radiating gass since the line of sight throught the layer is longer at larger angles.

Independent of the course of this difference we found that the measured sensitivety factor fitted better to the data than the calibration profile. When the calibration profile where applied to the data it gave higher intensities at the edges of the image than in the center. Since we doesn't have any dirrect use for calibrated intensities we use the measured flat-field correction for the rest of this study.

4.2 MSP

4.2.1 Interpolating missing MSP data

In the older MSP data, from before 2001, sometimes some short periods of data is missing. This was due to some sync problems with the MSP which made it skip recordings from time to time. When not taken care of this could result in sudden changes in the keograms. Since the MSP data contain time informations it is possible to find these regions lacking data. In figure (4.9) an MSP keogram from 26 of November 2000 is plotted. This is one of the more extreme cases when it comes to number of these jumps in data recording. Figure (4.9a) shows how this can be seen as vertical white stripes in the keogram. This makes it difficult to interpret visually.

To solve this problem we have chosen to interpolate the data along the time axis so it becomes evenly spaced. The resulting keogram can be seen in figure (4.9b). For the interpolation we used the built in function for one dimensional interpolation in MatLab set for linear interpolation. To simplify the data processing we didn't just interpolate the data in the areas where it was missing, we ran the interpolation function on the whole data set. That means we asked the function to give us data at certain evenly spaced times. If the time happened to be between two data points the function would give us a linear interpolation of those two points, that means the point that would be on a strait line in between those two points. As a time step for the interpolation we chose the sample frequency as the supposed scan frequency of the MSP. This

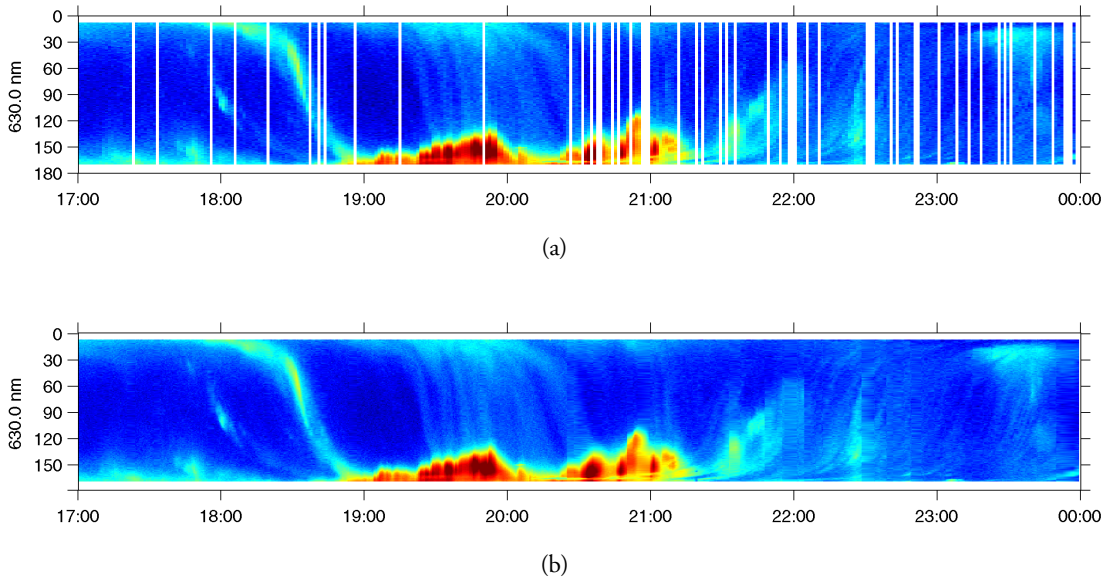

Figure 4.9: Meridian scanning photometer observation of 640.0 nm emission from Ny-Ålesund 26. November 2000. (a) The plot shown with the empty data left blanc. (b) The same MSP data as in (a) interpolated to an evenly spaced time axis

should make it sure that the resulting keogram doesn't deviate to much from the original data. If it should happen that time we ask for lies in between to ordinary data points the result would just be a value between the values of the two data points. This will act as a moderate mean filter and give rise to reduced single pixel intensitys peaks. In other words it will, in the worst case, act to reduce the noise, but will not affect the larger scale structures we are interested in here.

4.2.2 Locating the open-closed field line boundary (OCB)

Blanchard et al. (1995) describe a technique for locating the night time open-closed field line boundary (OCB) in 630.0 nm emission data. The background for this is that the separatrix seems to be mapped to areas in the in ionosphere slightly north of, but very close to the poleward edge of the 630.0 nm auroral emission. This poleward edge of the auroral emission can then be used as an estimate of the open-closed field line boundary. To locate this edge they suggested using least-square fit of a step function to the emission data versus latitude.

Blanchard et al. (1995) gave three criteria for accepting the step function fit as the poleward border of auroral emission:

1. The average polar cap intensity has to be low. Less than 300 R.
2. The step increase in the polar cap boundary is more than 75% of the polar cap intensity.
3. The correlation between the step function an the latitude profile is higher than 80%

Two of these three criteria has to be fulfilled. In addition the average polar cap intensity must be less than the average auroral intensity.

In our implementation of this method we had to rise the first criterium from 300 R to 1.4 kR because the polar cap patches contribute a lot to the polar cap intensities making it much higher than 300 R. Figure (4.10) shows one scan of MSP data taken in Ny-Ålesund 12.1.2002

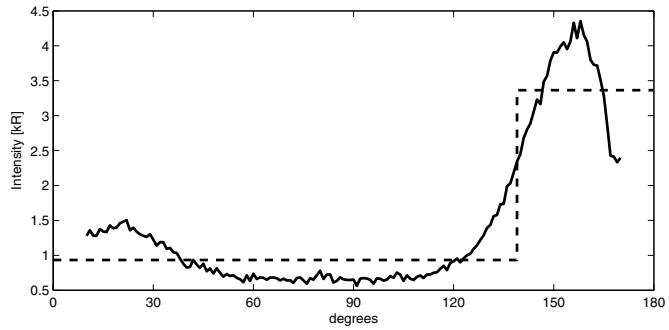

Figure 4.10: Step function fit to a MSP scan from NY-Ålesund 12.1.2002 at 18:07 UT. The solid line is the MSP scan and the dashed line is the step function fit.

at 18:07 UT together with the step function fit. As seen in this picture the average polar cap intensity could be as high as 1 kR or more. The polar cap patch, seen to the left in the figure goes as high as 1.5 kR in this case. It has to be mentioned that there has been some problems with the calibration on this data set so we are not absolutely sure that these intensity values are correct. The complete keogram for this day with the OCB marked can be seen in figure (4.11).

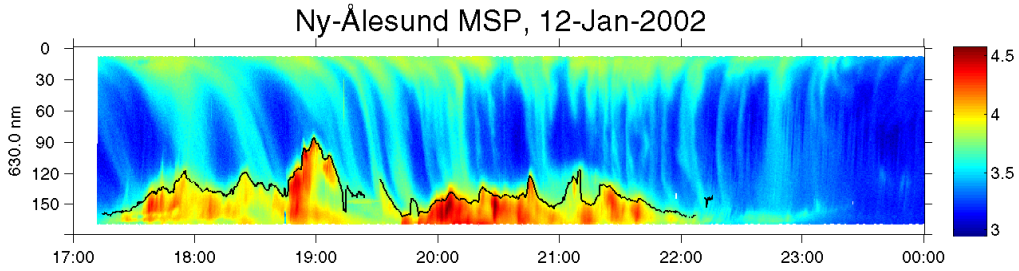

Figure 4.11: The Open-closed field line boundary traced in 630.0 nm MSP data from Ny-Ålesund 12.1.2002. The black line following the polward edge of the aurora represent the Open-closed field line boundary as fond by the methods described by Blanchard et al. (1995).

4.3 IMF

4.3.1 IMF averaging and delays

In this study we wanted to check our data for IMF dependence. But the measurements of the IMF is done $240 R_E$ away from Earth. To compare these measurements to effects in the ionosphere they need to be time shifted to the place we want to see the effect.

There exist several models for calculating time shift from a spacecraft to the ionosphere (Khan and Cowley, 1999; Ridley, 2000; Ridley et al., 1998). Here we have chosen a fairly simple one. The distance (along the X_{gsm} axis) is divided by the radial component of the solar wind speed ignoring any effects of the bow shock or magnetic structures differencing a lot in Y_{gsm} direction.

It is assumed that a structure in the solar wind is moving with it's solar wind speed all the way to the magnetopause. The time shift is then calculated as:

$$\Delta t = \frac{X_{gsm} - r_0}{V_x} \tag{4.20}$$

Where V_x is the solar wind speed component along the sun-earth line, and X_{gsm} is the x-component the satellite position in GSM-coordinates. r_0 is the magnetopause standoff at the sub solar point calculated using the empirical model by Shue et al. (1998) from the parameters IMF B_z and solar wind dynamic pressure.

$$r_0 = \left[10.22 + 1.29 \tanh\left(0.184(B_z + 8.14)\right)\right] D_p^{-\frac{1}{6.6}} \quad [R_E] \tag{4.21}$$

Where r_0 is in earth radii, and D_p is the solar wind dynamic pressure given in nanopascals.

$$D_p = N_p m_p V_x^2 \cdot 10^{21} \quad [\text{nPa}] \tag{4.22}$$

As an example we can use the measurements from 12. January 2002 (Figure 5.2). Taking average values for the time period 17:00 UT until 01:00 UT we get a average solar wind speed in the X-gsm direction, $V_x = 544\,\text{km/s}$, distance $X_{gsm} = 1.5447 \cdot 10^6$ km and average magnetopause stand off distance $r_0 = 10.2\ R_E = 6.50 \cdot 10^4$ km. This would then give a time shift of 2720 s or approximately 45 min.

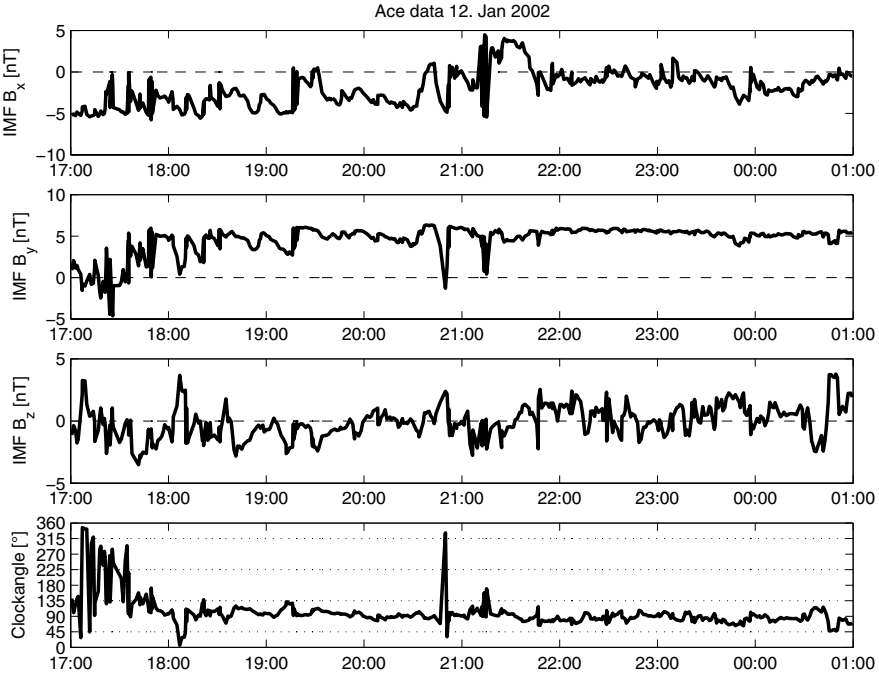

Figure 4.12: Timeshifted IMF for 12. January 2002.

Through our data set of patches we found r_0 varying from 7.1 – 12.09 R_E, giving a difference of 1.3 – 3.6 minutes to the delay time.

There exist different numbers for the ionosphere response time from a IMF change at the magnetopause depending on what methods you use (Ridley et al., 1998; Khan and Cowley, 1999). Most of them in the order of 10–25 minutes.

Hosokawa et al. (2006) found good correlation between IMF B_z and polar cap patch speed with a time shift of 44 minutes. Where 43 minutes was the estimated delay from the spacecraft to the magnetosphere, making the speed change almost instantaneously. The correlation

between IMF B_y and drift angle had a maximum at 66 minutes, and they suggested that this difference might be due to two different response mechanisms.

In our study we have chosen to use 30 minutes averages of the time shifted IMF data preceding the patch observation. This is approximately the same averaging as used in statistical studies of convection patterns (Ruohoniemi and Greenwald, 1996, 2005; Weimer, 1995). In addition this should cover both the B_z and the B_y response as seen by Hosokawa et al. (2006). We did a test using one hour averaging and found that it didn't change the statistics significantly.

4.4 Analysis of MSP data

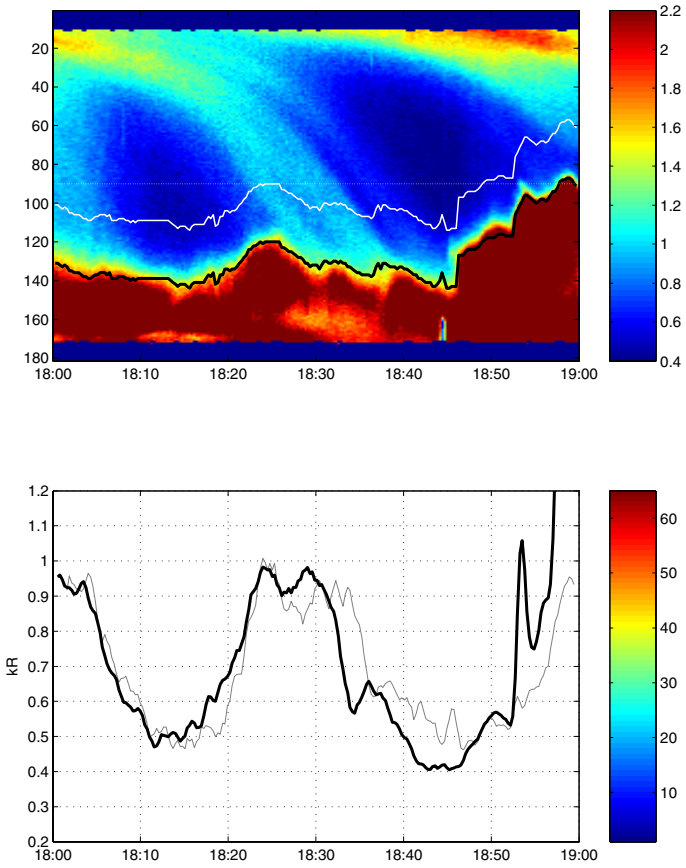

Figure 4.13: A plot of one hour MSP data from 12. January 2002. The black curve in the upper image is the OCB found by the technique described in section 4.2.2. The white curve lies 30°north of the OCB. The intensities along this curve is plotted as the gray curve in the lower image. The black curve in the lower image is the the intensities measured at zenith, represented by a white dotted line in the upper image. All intensities are given in kR, and the times are given in UT. Between 18.30 and 18.40 UT a polar cap patch are seen crossing OCB an entering the aurora.

All available MSP for the time period 15.00 – 02.00 UT from the years 1998 – 2005 has been checked for any signs of polar cap patches. In MSP keogram polar cap patches are most often seen as inverted S-shaped trails in the 630.0 nm channel with intensities lower than the aurora, but still higher than the background. In figure (4.11) these typical trails can be seen. These trails in the keogram are made when a polar cap patch drift over the MSP along the magnetic meridian from north to south. The patches are registered when they are seen to enter the open-closed field line boundary. Lorentzen et al. (2004) observed that polar cap patches merge into

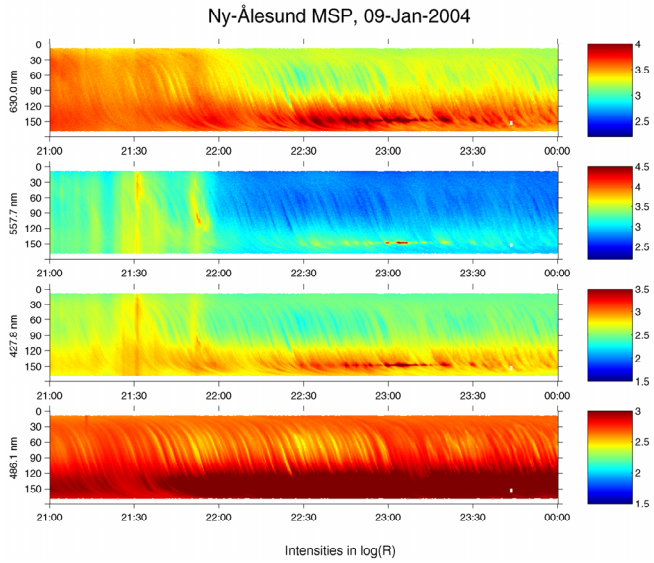

Figure 4.14: The effect of patchy (tropospheric) clouds in a MSP keogram.

a brightening of the boundary of 630.0 nm emission. These auroral boundary intensifications can also be used as indicators of polar cap patches.

In our statistic we have only counted patches that are seen to enter the open-closed field line boundary. Patches that drift across the MSP scan line but disappeared out of sight before they gets to the OCB are left out. This way we can be sure that the patches we see are indicators of reconnection.

The MSP data was analyzed manually by looking at 1 hour MSP plots and the patches was registered with the time it crossed the open-closed field line boundary (OCB) with an accuracy to the nearest 5 minutes. All the dates and times of patches where then written to a file for later possessing by MatLab. Figure (4.13) shows one such one hour plot. The upper panel shows the actual keogram and the lower panel shows two profiles used to check the actual intensities. We used the criteria that the intensity of patches had to be more than 50% of the background intensity (Crowley, 1996), althought in some cases it was difficult to identify the actual background intensity.

4.4.1 Other signatures that can be mistaken for patches

There are other phenomenon's that make trails in the MSP keograms that can be mistaken for polar cap patches. Figure (4.14) and figure (4.15) shows some of these trails. The way to separate between these an polar cap patches are the fact that polar cap patches are mainly visible in the 630.0 nm channel, and only some times vaguely visible in 577.0 nm, these other phenomenon's are visible in more channels.

In figure (4.14) we see the effect of patchy clouds passing over the MSP scan line. In this case the clouds seems to be drifting more or less along the magnetic meridian creating the same inverted S-signature as expected by a polar cap patch. There are at least two factors that make these clouds visible to the MSP. The first is that they reflect light pollution from the settlement in Ny-Ålesund. This give rise to broad spectered radiation seen in all channels. The second factor is that there seems to be some auroral activity going on, and this aurora is diffused by the clouds.

In figure (4.14) we can see some brightening at 21.30 and 21.50 UT in the 5577.0 nm and the 427.8 nm channel, and there seems to be some aurora to the south for most of the time. If we where only watching the 630.0 nm channel it would be difficult to identify this as clouds. But it is even then signs to look for that reveals that this is not polar cap patches. The clouds give a totally different signature when it passes over the aurora. While the polar cap patches are connected with a brightening in the in the aurora, the passing of a cloud scatter the auroral light and gives a trail of lower intensity in the keograms. So the signature of a cloud in the 630.0 nm channel is that it has higher intensities than the background, but leaves a trail of lower intensities when it pases the aurora.

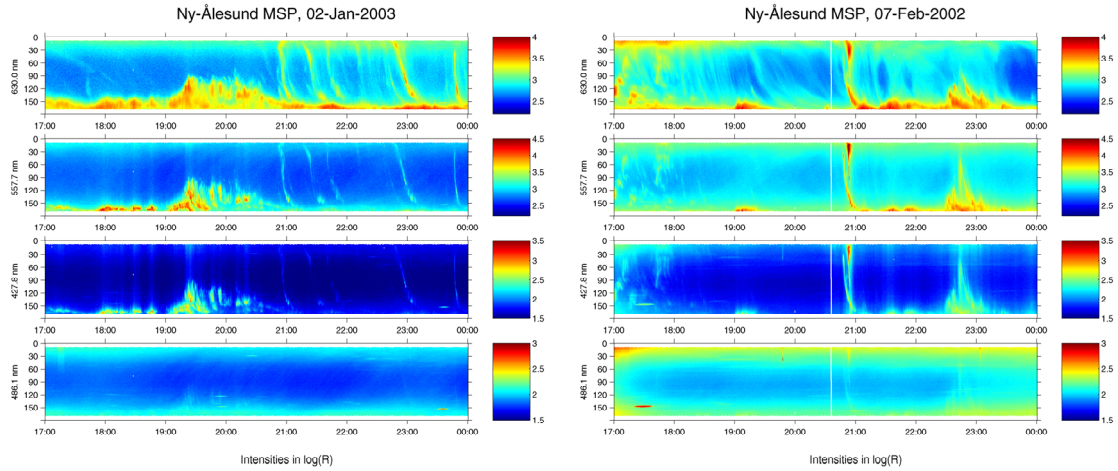

(a) (b)

Figure 4.15: Polar auroral arcs seen in MSP keograms.

Another phenomenon that sometimes causes inverted-S like signatures are polar arcs, some times also called sun-aligned arcs. These are related to velocity shear in the F region convection and are characterized by particle precipitation (Sandholt et al., 2002). Polar arcs are most common for IMF $B_z > 0$, but has been observed under $B_y > 0$ dominating condition also (Dyrland, 2005).

Since polar arcs are due to precipitating particles we would expect them to be visible in more of the MSP channels not only the 630.0 nm. Figure (4.15) shows two examples of polar arcs in MSP keograms. In (4.15a) polar arcs are visible between 21.00 and 24.00 UT. Weak patterns of the same type also seen in the 577.0 nm and the 427.8 nm channel. In figure (4.15b) a polar arc is seen at around 21.00 UT. This arc actually has a stronger signal in the 577.0 nm channel than in the 630.0 nm and it is even slightly visible in 486.1 nm. Before and after the arc we can see polar cap patches that doesn't leave trails in all these other channels.

Chapter 5

12. January 2002 – a comparison between MSP data and all-sky images

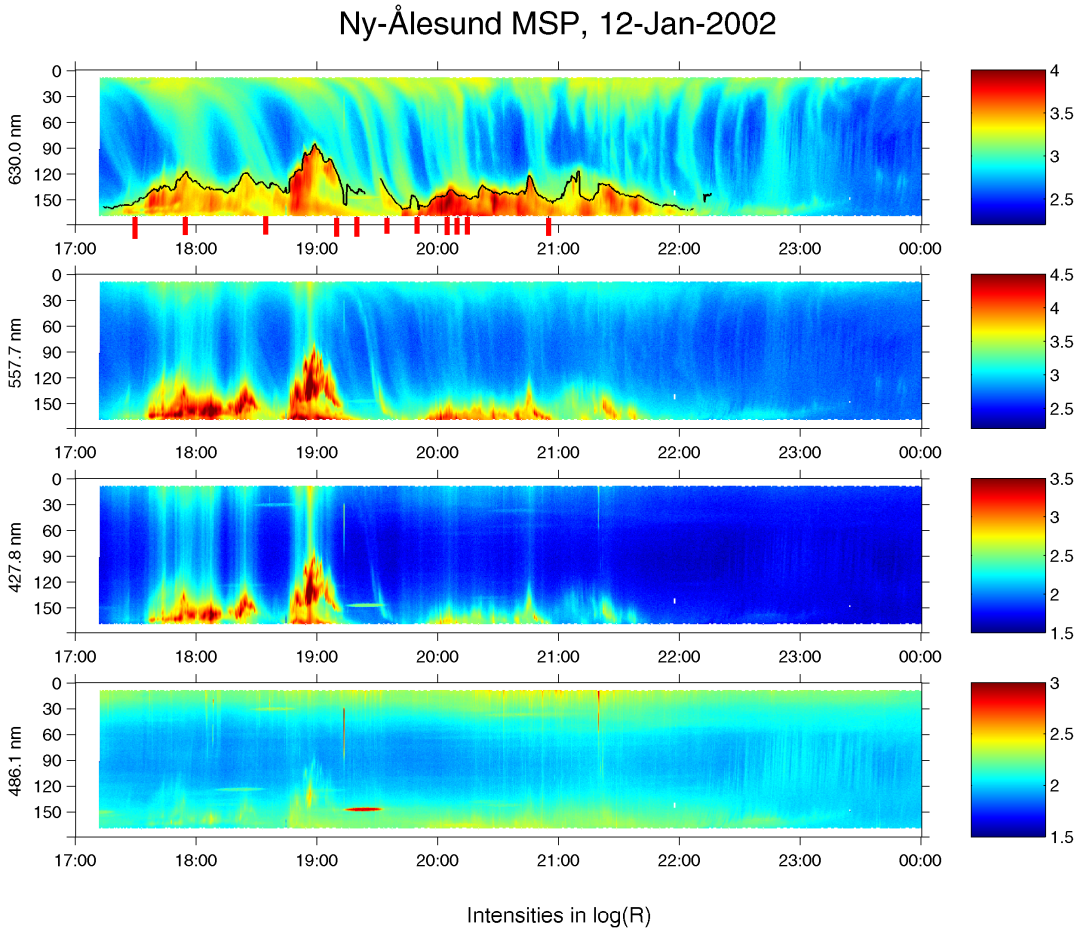

Figure 5.1: MSP keogram for 12. January 2002. The black line in the 630.0 nm channel represent the open-closed field line boundary, and the red marks along the axis of the 630.0 nm channel are registrations of patches crossing OCB. The time is given in UT

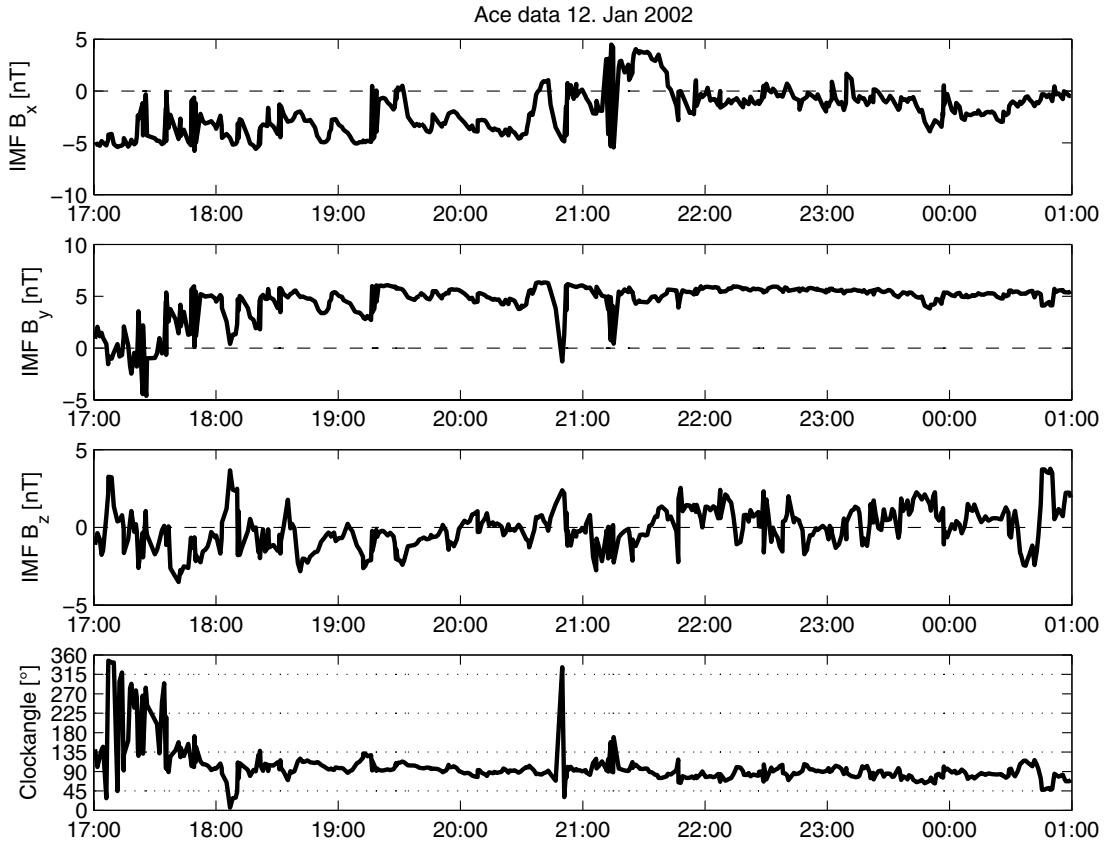

Figure 5.2: Timeshifted IMF for 12. January 2002.

In this chapter we are going to compare a day of MSP measurement with all-sky camera images to show the complex structures that give rise to the relatively simple inverted S-signatures in the MSP keograms. We will also try to relate this to the interplanetary magnetic field and the ionospheric convection.

If all patches had been perfectly circular or oval shaped in area having a uniform intensity and moving along the magnetic meridian with a constant speed, it would be no problem detecting them with the meridian scanning photometer (MSP). This is not the case.

As our observation site rotates under the ionospheric convection and as the convection pattern changes, the polar cap patches will cross our MSP scan line with different angles.

12. January 2002 is a fairly good date to use as example. We got MSP measurement from about 17.20 until way past midnight. The patch trails in the 630.0 nm channel are strong and easy to detect and we got all-sky images from two different cameras.

The first patch registered in the MSP data was at 17.30 UT (figure 5.1) but none of the cameras where operating at that time.

The first all-sky image is at 17.36 UT and is plotted in figure (5.5c) together with the convection pattern derived from SuperDARN. There are no patches seen at this time which might be related to the fact that the IMF B_z just has been positive (figure 5.2), and is changing rapidly. From the SuperDARN measurements the plasma flow seams to be going from the auroral oval toward the polar cap.

At 17.45 UT a polar cap patch is observed by the all-sky cameras (figure 5.3 and 5.4) northvest of Svalbard, directly at the northern part of the MSP scan line. This can then also be seen in the MSP keogram (figure 5.1), and at 18.00 UT we can see it going into a brightening in the aurora. By this time the IMF component has turned positive and is more or less going to keep this direction for the rest of the time (figure 5.2). After the patch has entered the aurora, the aurora seams to retreat for a while (figure 5.3), at the same time the next patch is already coming closer. Also this one going into a brightening at 18.35 UT.

Between 19.00 and 19.15 UT there is a sudden change in the drift direction of the patches from southeastward to southward. They also seems to change shape and get thin in the drift direction and longer perpendicular to the drift direction (figure 5.3 and 5.4). At 19.30 UT there is a small auroral brightening in the eastern part of one of patches while the patch is moving southwards. This same situation can be seen in figure (5.5f) where it looks like plasma is moving eastwards at the same time as the patches optically is moving southwards.

The change of patch drift direction continues to change even after 19.30 UT although a bit slower and by 21.00 they cross the MSP scan line perpendicularly and are no longer seen enter the open-closed field line boundary (OCB) in the MSP keogram. After 22.00 the aurora also disappears from the field-of-view of the MSP and the all-sky cameras. Even after that some weak patches are seen to cross MSP scan line. Mostly perpendicular to it.

As seen to this example both the patch drift direction and the location of the auroral boundary seems to be rotating as the observation site rotates under the convection system. Fortunately the patches are often long in the direction perpendicular to their drift direction and that is the reason why they in most cases makes these inverted S-shapes in the MSP keograms even when they drift width a large angle to the magnetic meridian.

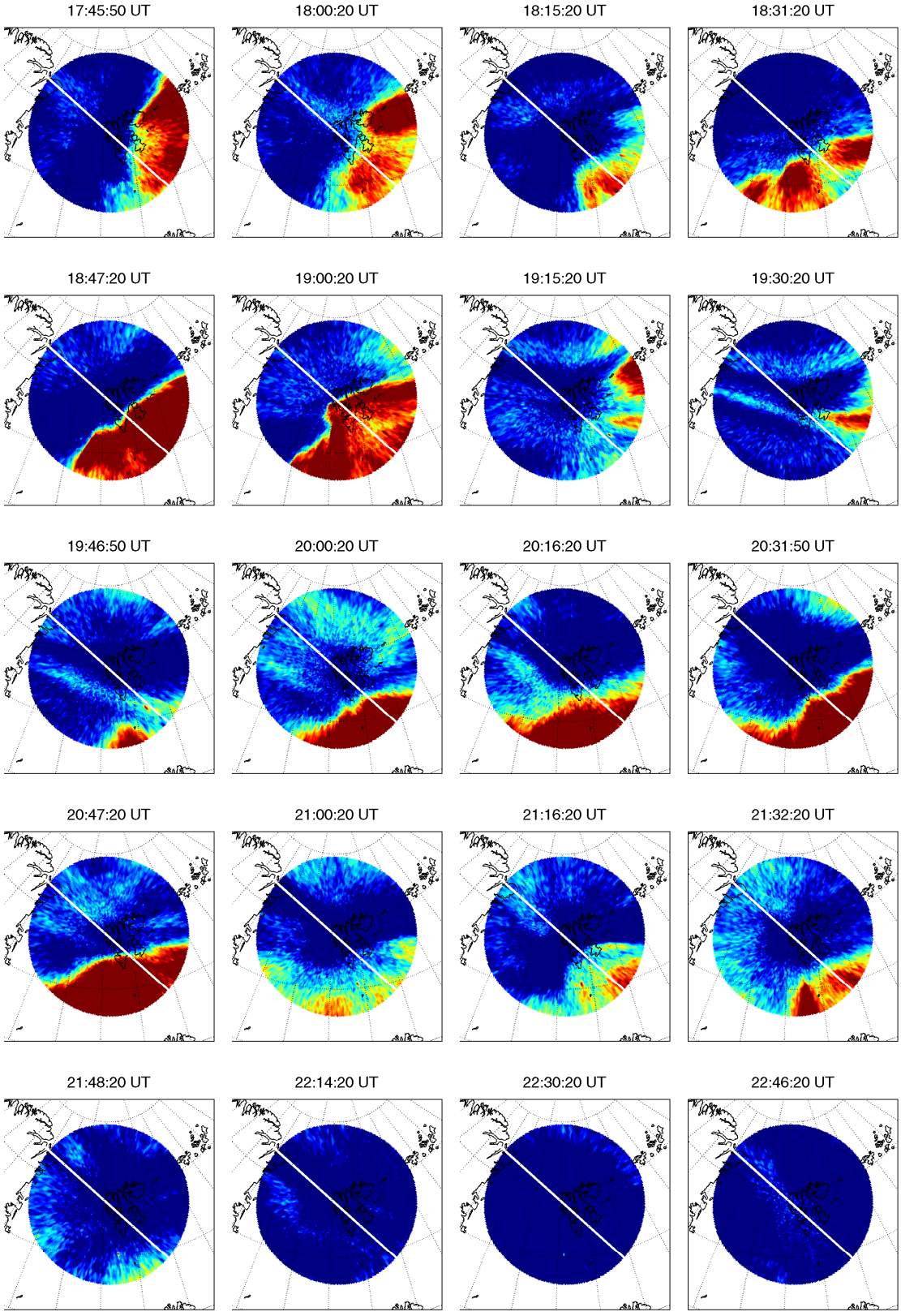

Figure 5.3: All-sky images from the UiO camera in Ny-Ålesund 12. January 2002, covering 17.00 – 22.46 UT with 15 minutes intervals. The white line crossing the images represent the MSP scan line.

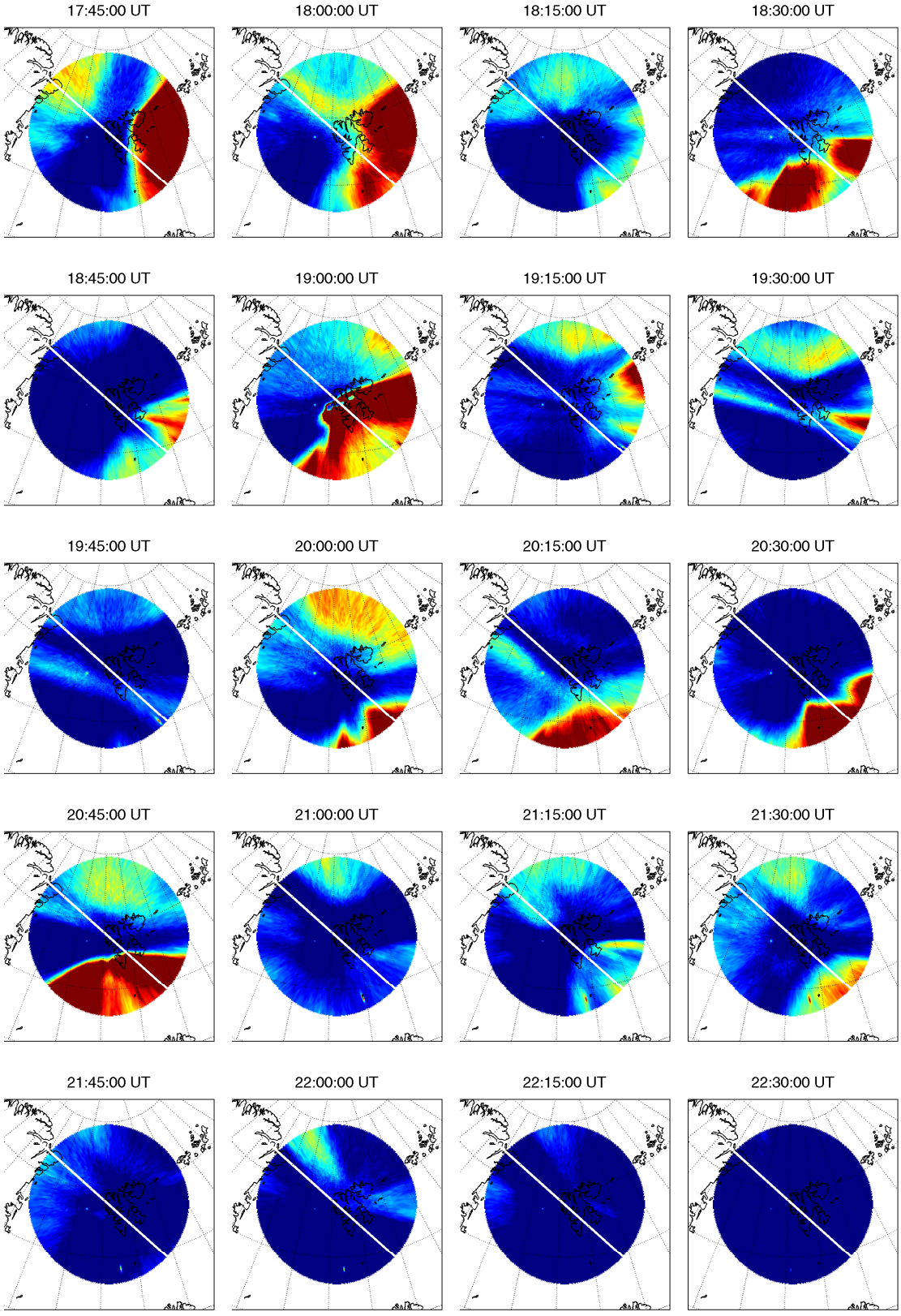

Figure 5.4: All-sky images from the AFRL camera in Ny-Ålesund 12. January 2002, covering 17.00 – 22.46 UT with 15 minutes intervals. The white line crossing the images represent the MSP scan line.

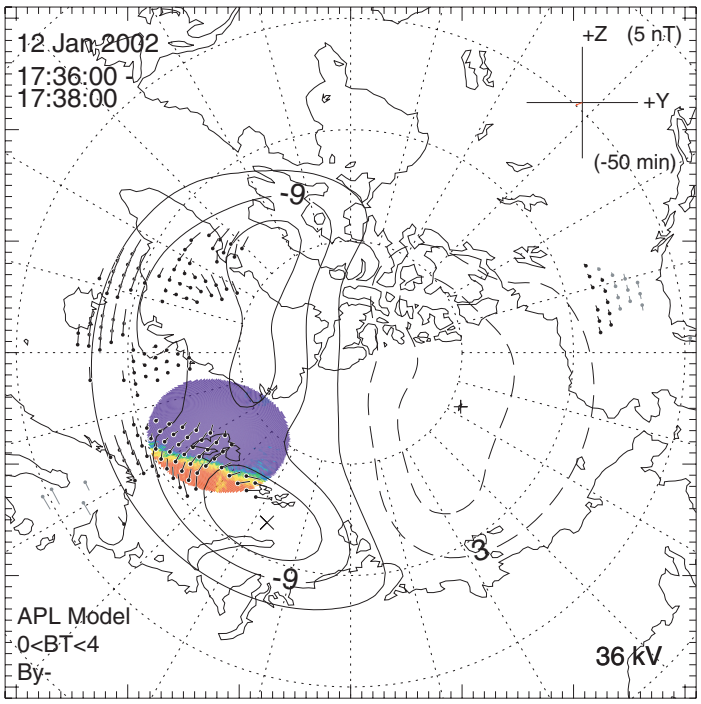

(a)

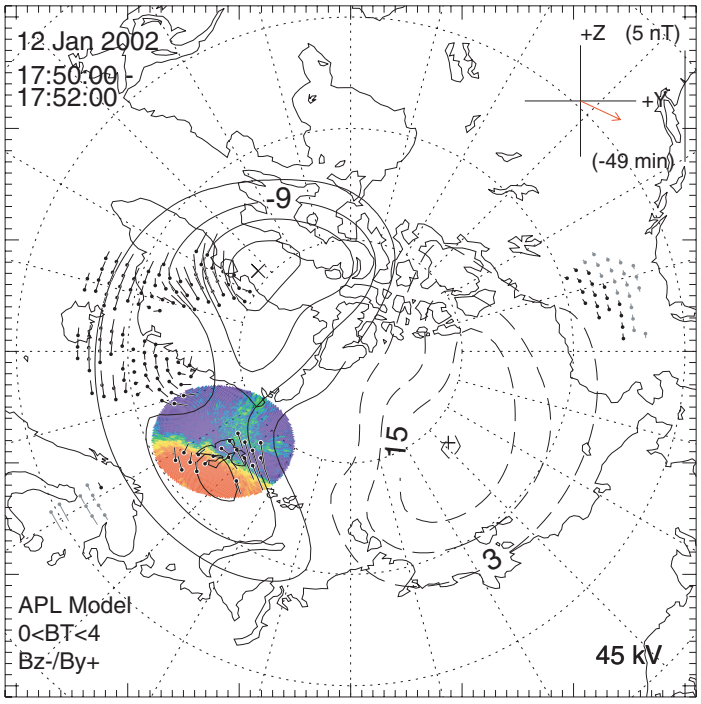

(b)

Figure 5.5: All sky images from the UiO camera plotted in a SuperDARN plot.

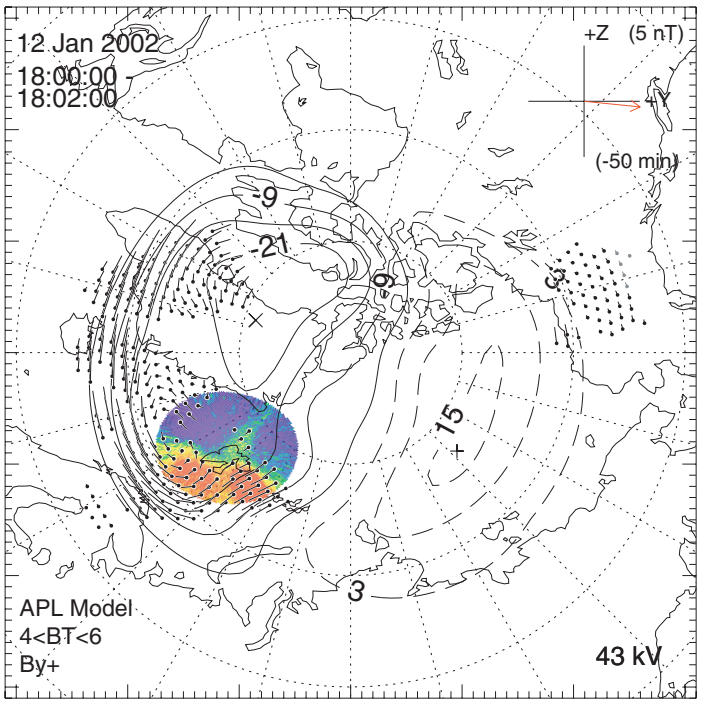

(c)

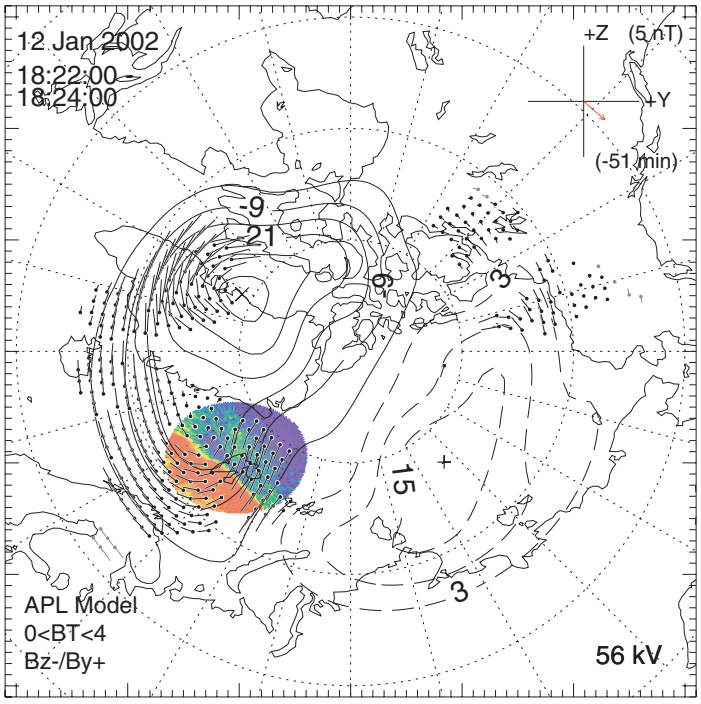

(d)

Figure 5.5: All sky images from the UiO camera plotted in a SuperDARN plot.

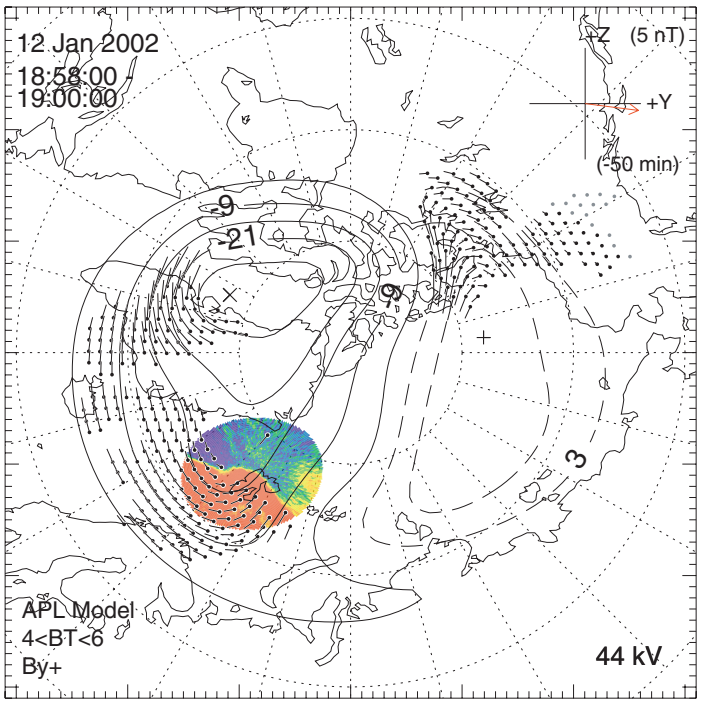

(e)

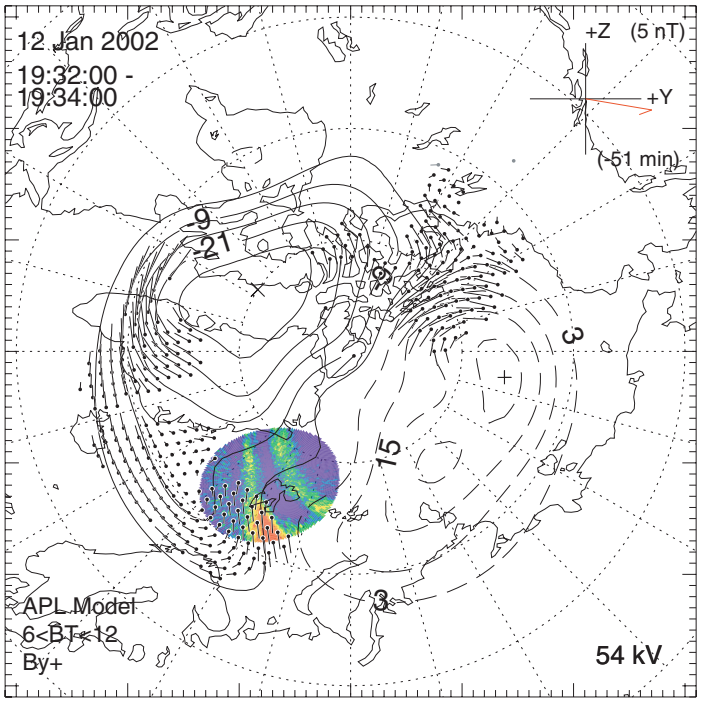

(f)

Figure 5.5: All sky images from the UiO camera plotted in a SuperDARN plot.

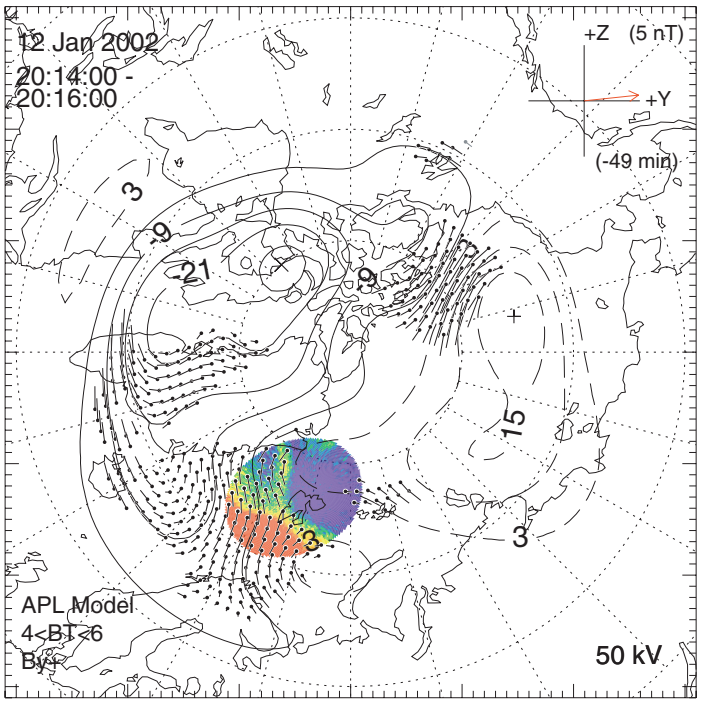

(g)

Figure 5.5: All sky images from the UiO camera plotted in a SuperDARN plot.

Chapter 6

Statistics

For this statistics we used meridian scanning photometer (MSP) measurements from Ny-Ålesund. The operating season for the MSP goes from mid November until mid February, and due to it's light sensitivity it is not operated unless both the Sun and the Moon is more than 10° below the horizon. In addition the instrument needs a certain degree of clear sky to give useful measurements as seen in section 4.4.1 in chapter 4. This puts some strict regulations on the amount of data available for this statistic. A survey of the available data from the years 1998 until 2005 are shown in figure (A.1) in appendix A. The red marks in the figure are times when patches has been observed.

6.1 Patch occurrence

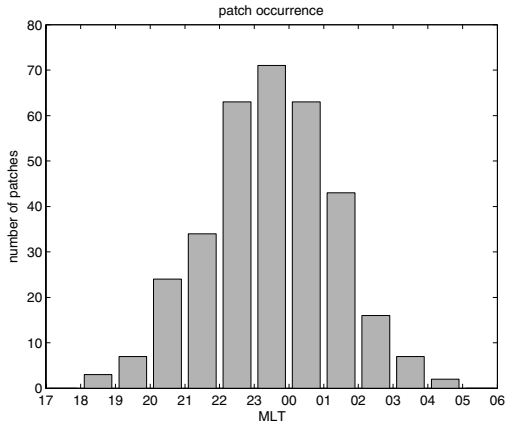

Figure 6.1: The polar cap patch occurrence over Ny-Ålesund as a function of magnetic local time.

Going trough 8 years of MSP data from 1998 until 2005, we found 43 days where patch activity could be identified. These days and the times patches where observed crossing OCB are listed in table (A.1) in appendix A. In total we observed 333 patches crossing the nighttime open-closed field line boundary (OCB). These OCB crossings where registered with the UT-time to the nearest 5 minute period. The UT-time was then converted to magnetic local time using 20.50 UT as magnetic midnight. Sorting this data in one hour bins MLT time we got the distribution shown in figure (6.1). Figure (6.2) shows how the distribution would be if UT time is used instead of MLT.

Polar cap patches was observed from 18.30 – 04.50 MLT (15.20 – 0.40 UT) with an average time of 23.25 MLT (20.14 UT).

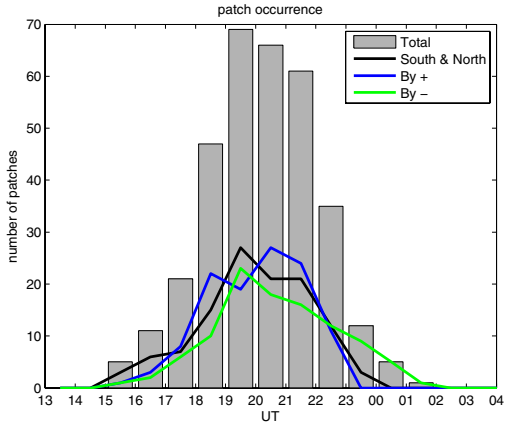

Figure 6.2: The polar cap patch occurrence over Ny-Ålesund as a function of universal time. The IMF conditions are sorted after the same clockangle criteria as in figure (6.5c).

6.2 IMF dependence

The shape of the convection pattern in the ionosphere is strongly dependent upon the magnetic field in the solar wind (IMF). Since polar cap patches are following this convection we could expect an IMF dependence on the patch occurrence distribution. To investigate this we have to separate our patch occurrence data into different categories depending on the IMF. For IMF data we use 30 minutes averages of ACE data preceding the OCB crossing as described in section 4.3. Statistical studies of ionospheric convection (Ruohoniemi and Greenwald, 1996, 2005; Weimer, 1995) and particle precipitation regions (Newell et al., 2004) uses quite many categories. Ruohoniemi and Greenwald (1996, 2005) and Weimer (1995) ends up with 24 categories, separating on clockangle and total IMF, while Newell et al. (2004) only uses 4, separating on B_y and B_z condition.

Due to our fairly low number of patches (only 333) we had to keep the number of categories low for the statistics to make any sense at all. We decided upon using only 3 categories. We used clockangle as the separation criterium. Clockangles between 45°an 135°was asigned to B_y+ and clockangles between 225°and 315°was asigned to B_y- the rest where assigned in the "north & south" category. Figure (6.4) shows a plot of IMF B_z versus IMF B_y for all patch observations used in this study. The different colors shows the different categories the observation has fallen in. Green is for B_y-, blue is for B_y+ black is for "north & south". The result of this separation by clockangle can be seen in figure (6.3)

Table (6.1) lists the min, max and mean times for these distributions.

Figure (6.5) shows the effect of using other sorting criteia. In figure (6.5a) the observations where sorted according to the B_y. We tried to match the categories used by Newell et al. (2004), with separation on $B_y = -3$ and 3 nT. Figure (6.5b) shows where the differnet categories falls in a clockangle plot.

In figure (6.5e) still uses a clockangle separation only the north and south sectors are shrunken so that more of the observations goes eighth to B_y+ or B_y-. The separation angles here is 22.5°, 157.5°, 202,5° and 337.5° as seen in figure (6.5f).

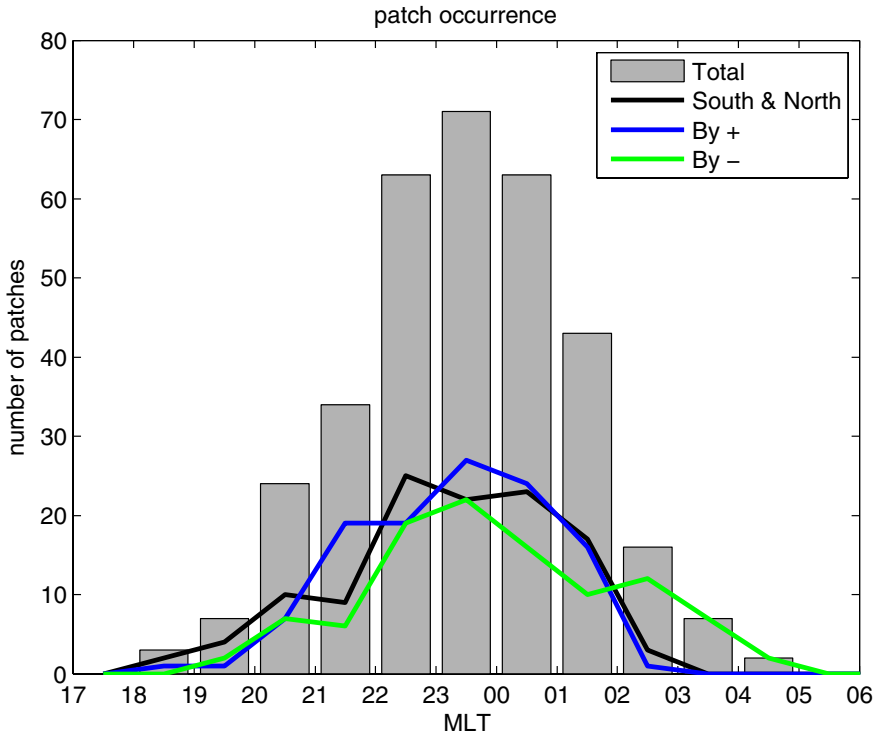

Figure 6.3: The polar cap patch OCB crossings over Ny-Ålesund as a function of magnetic local time.

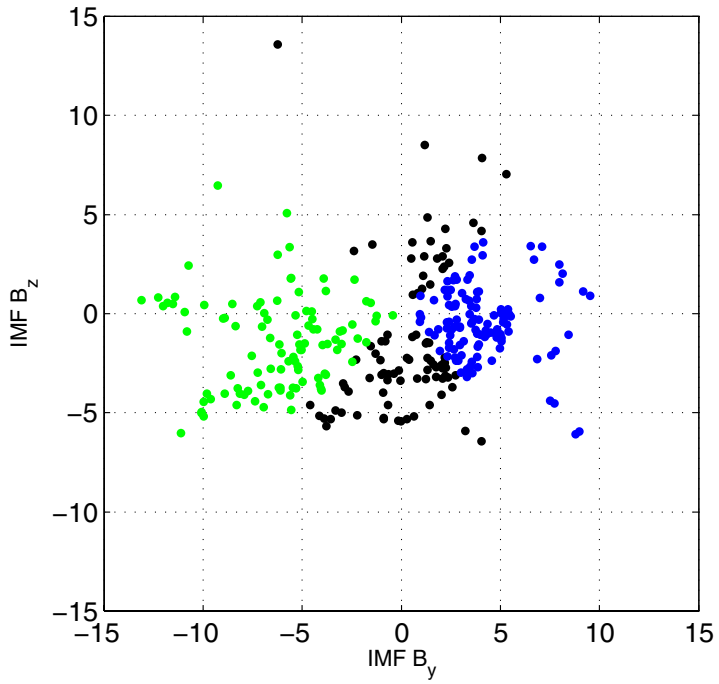

Figure 6.4: IMF vector in the GSM Y-Z plane

		IMF dependence		
	Total	B_y+	North & south	B_y-
Mean	23:25	22:48	23:26	23:56
Min	18:30	18:30	18:30	19:05
Max	04:50	01:50	02:40	04:50
Number	333	115	103	115

Table 6.1: Mean, min and max times for patch OCB crossing for different IMF conditions.

None of these sorting methods seems to give any better result than the first methode.

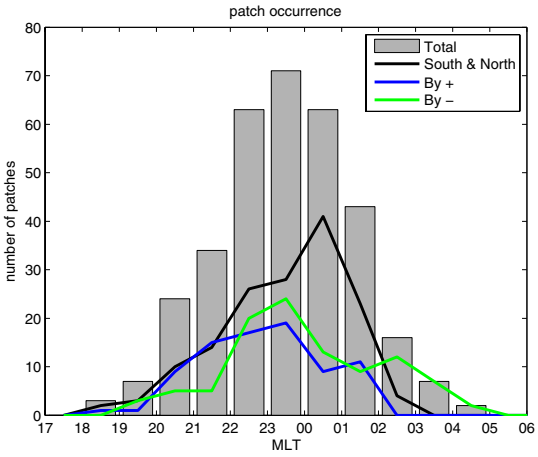

(a) separating at $B_y = -3$ and 3 nT

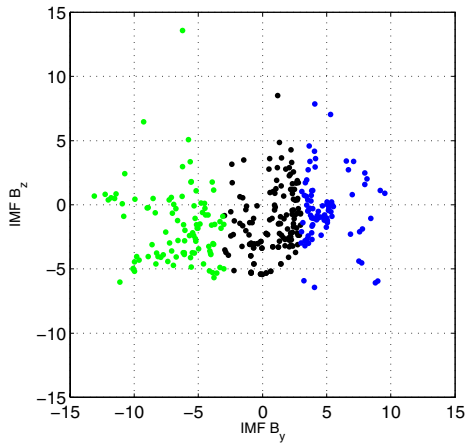

(b) IMF vector in the GSM Y-Z plane

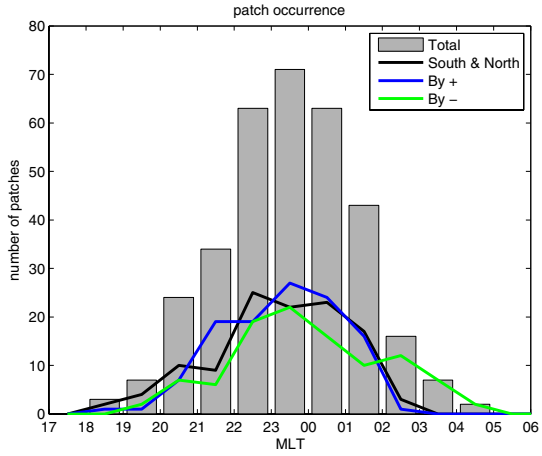

(c) Separating at clockangle 45°, 135°, 225° and 315°

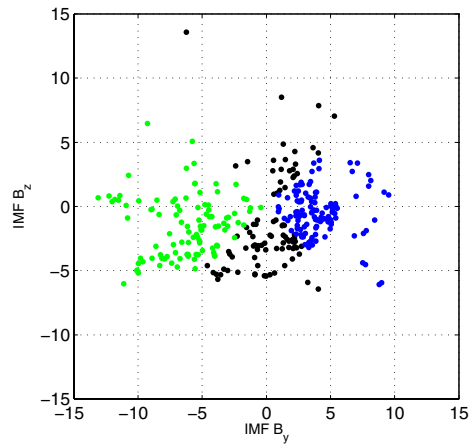

(d) IMF vector in the GSM Y-Z plane

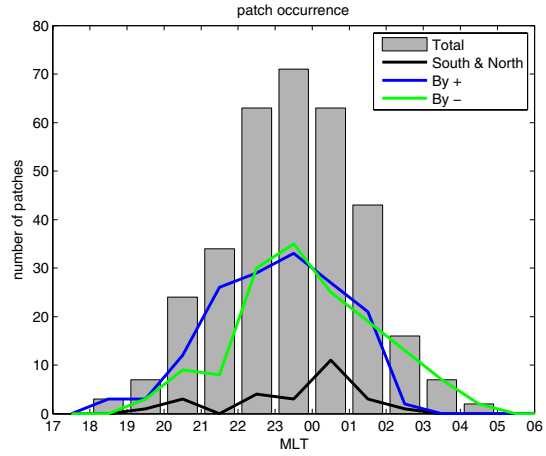

(e) Separating at clockangle 22.5°, 157.5°, 202,5° and 337.5°

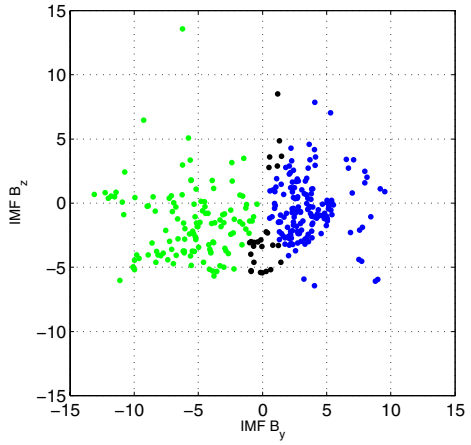

(f) IMF vector in the GSM Y-Z plane

Figure 6.5: A comparison of the IMF dependence on patch occurence using different IMF clases.

Chapter 7

Discussion and conclusion

There are two distinct results from our statistical study:

1. Polar cap patches was found to cross the night side OCB over Svalbard in the interval 18:30 – 04:50 MLT with an average of 23:25 MLT, more than half an hour before magnetic midnight. In our histogram the highest occurrence of patches was in the hour before magnetic midnight.

2. The changes in IMF B_y seems to be able to move the area where patches crosses the OCB by $\sim$ 1 hour MLT.

In our statistic there seem to be a small dawn-dusk asymmetry in the patch OCB crossings. Of the 333 patches found in our material 202 patches where found to cross the OCB before magnetic midnight. That is almost 2/3 of the patches.

There are different factors that can contribute to this asymmetry. It could be an expression for a general asymmetry in the convection pattern. It is also possible that earth's dipole tilt make some MLT sectors more favorable for production of polar cap patches. The dipole tilt will favor some MLT sectors when it comes to the access to high electron density plasma. In sectors where the convection throat goes further geographic south than others, it will get plasma that has received more solar radiation. If this can explain our asymmetry is not yet clear.

An other explenation could be asymetries in magnetotail phenomenons. A statistic of tail passings by the satellite Wind (Raj et al., 2002) finds an dawn-dusk asymmetry in the occurrence of bursty bulk flows where most events occurred in the premidnight sector. Lyons et al. (1999) found a relation between bursty bulk flows and poleward boundary intensification in the ionosphere. And poleward boundary intensification seems to be strongly linked with polar cap patch OCB crossing (Lorentzen et al., 2004).

Appendix A

Patch observations in the Ny-Ålesund MSP data

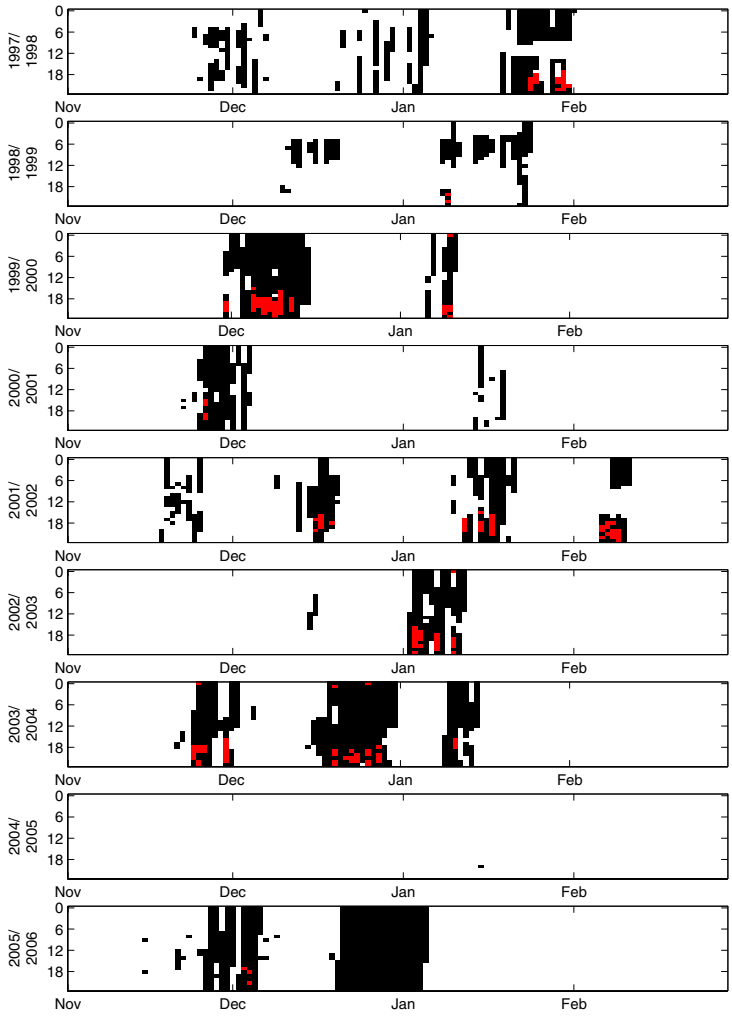

Figure A.1: Aviable MSP data. The red marks are times when patches have been observed.

Date	#patches	first	last
1998			
24-Jan-1998	5	19:50	22:30
25-Jan-1998	5	18:55	20:05
29-Jan-1998	6	19:30	22:40
30-Jan-1998	9	17:35	22:35
31-Jan-1998	2	21:10	21:30
1999			
09-Jan-1999	6	20:40	22:50
30-Nov-1999	12	19:20	21:50
05-Dec-1999	12	15:20	21:55
06-Dec-1999	7	18:10	20:35
07-Dec-1999	15	18:10	22:05
08-Dec-1999	16	18:00	21:55
09-Dec-1999	9	19:50	23:30
10-Dec-1999	18	16:35	22:40
12-Dec-1999	5	18:15	21:00
2000			
09-Jan-2000	4	20:55	22:30
10-Jan-2000	9	20:10	00:40
26-Nov-2000	6	15:55	20:30
2001			
16-Dec-2001	4	17:20	20:40
17-Dec-2001	7	16:35	19:10
19-Dec-2001	1	18:40	18:40

Date	#patches	first	last
2002			
12-Jan-2002	11	17:30	20:55
15-Jan-2002	9	15:20	20:55
17-Jan-2002	11	16:55	21:55
06-Feb-2002	4	19:45	22:25
07-Feb-2002	7	18:35	21:40
09-Feb-2002	13	20:45	23:10
2003			
03-Jan-2003	16	16:40	23:45
04-Jan-2003	4	17:35	21:40
07-Jan-2003	11	18:40	22:50
10-Jan-2003	11	19:20	00:50
24-Nov-2003	8	18:45	21:50
25-Nov-2003	6	18:50	00:20
26-Nov-2003	3	18:55	19:50
30-Nov-2003	15	16:55	22:15
20-Dec-2003	6	19:50	01:40
22-Dec-2003	1	21:20	21:20
23-Dec-2003	3	19:05	22:55
24-Dec-2003	3	20:25	22:40
26-Dec-2003	5	19:50	00:15
28-Dec-2003	7	18:40	22:55
2004			
11-Jan-2004	7	16:50	18:55
2005			
03-Dec-2005	2	17:30	17:40
04-Dec-2005	2	18:25	21:15

Table A.1: Dates used in the patch statistics

Appendix B

Program codes

All of the folloving programs has been made in MatLab 7.1. Some of them are using the mapping toolbox.

webdist_NYA_v2_m6.m

This program is used to make a map projection of the all-sky images. It is originally written by Espen Trondsen, but is modified and revised by Njål Gulbrandsen. The most important changes is a correction of the calculation of the horizontal angle in the projection algorithm, the addition of corrections for a curved Earth and the addition of a line marking the MSP scan line.

The Mapping Toolbox in MatLab is used to do the final computations of the coordinates.

```
function [lats, lons]=webdist_NYA(in_file, header)
% Function originaly writen by Espen Trondsen
% Modified by Njål Gulbrandsen

load nya_info_pmis;

% Checking the calibration data for camera rotation
ang_nr = find(site_info.rot_date < header.time);
ang = site_info.cam_rot(ang_nr(length(ang_nr)));
rot=ang+45;

site_lat = 78.92; %Site posission
site_lon = 11.95;

cla;

filter =1;

if header.wavel=='557.7nm'
    filter = 2;
elseif header.wavel=='630.0nm'
    filter = 1;
end

switch filter
    case 1 % 630.0 nm filter
        altitude = 300; % Project aurora to altitude (km)
    case 2 % 557.7 nm filter
        altitude = 120;
```

```
    case 3
        altitude = 120;
    case 4
        altitude = 120;
    case 5
        altitude = 250;
end % switch filter

Re =6.37e3; %Earth radius in km
angle = 70; %Maximal view angle
a=-angle:(140./(size(in_file,1)-1)):angle;

% Assigning x and y coordinates(later used to calculate angle)
x=a;
y=x;

% Calculating view angle for every pixel
X=repmat(NaN, length(a));
for i = 1:length(a)
    for j=1:length(a)
        X(i,j)=sqrt(a(i).^2 + a(j).^2);
    end
end

% Calculating distance from center by project the image to a certain altitude
X=altitude.*tand(X);

% Correct for Earth's curvature
curv_earth=true;
if curv_earth
    alp=atan(X./altitude);
    X=Re.*(alp-asin((Re.*sin(alp))./(Re+altitude)));
end

lats=NaN.*ones(length(a)); %Matrixes for latitude and longitude info
lons=NaN.*ones(length(a));

% Geting latitude and longitude information from displasement angel and
% direction
[lats, lons] = reckon( repmat(site_lat, size(X)), repmat(site_lon, size(X)), km2deg(X),
    ...
    rot+180./pi.*atan2(repmat(x,size(X,1),1), repmat(y',1,size(X,2))) );

axesm('eqdazim'); % Define map projection: eqdazim - EQuiDistantAZIMutal

gridm('Origin', [site_lat site_lon], ... % "center" - to avoid stretching of plot
    'MLineLocation', 10, ... % Distance between meredians (degrees)
    'MLineLimit', [0 85], ... % Limits for meridian-plotting (degrees latitude)
    'MLineException', [0 30 60 90 150 180 -150 -120 -90 -60 -30], ... % Meridians xing N-
        pole
    'PLineLocation', 5); % Distance between latitudes (degrees)

set(gca, 'XLim', [-0.135 0.135], 'YLim', [-0.135 0.135]);

n = in_file;
lats= flipud(lats);
lons = flipud(lons);

% Plots the all-sky image
```

```
pcolorm(lats, lons, n),...
   shading interp;% colorbar;

%Plotting coastline
load mycoast;
plotm(lat, long, 'k');


d = tan(70.*pi./180).*altitude-100;
dirrect= -48;

%Plotting magnetic meridian (MSP scan line)
[gclat1,gclong1] = reckon('gc',site_lat,site_lon,km2deg(d),dirrect);
[gclat2,gclong2] = reckon('gc',site_lat,site_lon,km2deg(d),180+dirrect);
plotm([gclat1 gclat2],[gclong1 gclong2],'w','linewidth',1.5);
```

webdist_NYA_v2_m_map.m

This program is a version of webdist_NYA_v2_m6.m that uses the freely available M_Map package (available at `http://www.eos.ubc.ca/~rich/m_map1.4.zip`). This is useful for computers that doesn't have the Mapping toolbox installed. Only the last part of the code differs from webdist_NYA_v2_m6.m and it's only this part that is shown here.

```
...
% Geting latitude and longitude information from displasement angel and
% direction
[lons,lats,a21] = m_fdist(repmat(site_lon, size(X)),repmat(site_lat, size(X)),...
      rot+180./pi.*atan2(repmat(y,size(X,1),1),repmat(x',1,size(X,2))),X.*1000);

m_proj('Azimuthal␣Equidistant',... % Define map projection
       'lon',11.95,'lat', 78.92,...
       'rad', 12,'rec','on');

 set(gca, 'XLim', [-0.15 0.15], 'YLim', [-0.15 0.15]);

n = in_file;
[Xcor,Ycor]=m_ll2xy(lons,lats);

% Plots the all-sky image
pcolor(Xcor,Ycor, flipud(n)),...
    shading interp,colorbar;

%Plotting coastline
load mycoast;
m_line(long,lat,'color','k');

title(datestr(header.time));
m_grid('box','on','xticklabels',[],'yticklabels',[]);
axis equal;

d = tan(70.*pi./180).*altitude;
dirrect= -48;

%Plotting magnetic meridian (MSP scan line)
[gclat1,gclong1] = m_fdist(site_lon,site_lat,dirrect,d.*1000);
[gclat2,gclong2] = m_fdist(site_lon,site_lat,180+dirrect,d.*1000);

hold on
```

```
m_plot([gclat1 gclat2],[gclong1 gclong2],'w','linewidth',2);
hold off
```

webdist_NYA_v2_am.m

This program is a modified version of webdist_NYA_v2_m6.m that is used to plot the images from AFRL-camera in Ny-Ålesund. There is only some Small changes done to the program. The first is:

```
rot=90;
```

Then this camera has been calibrated for angular dependence, and this is implemented by adding the following code in front `X=altitude.*tand(X);`

```
elseif strcmp(proj,'am')
    b=284/2;
    c=-29/2;
    r_length=X.*(size(in_file,1)-1)./140;
    rpix= b.*sin(a./180*pi)+c.*sin(2.*a./180*pi);
    rpix=rpix./max(rpix).*size(in_file,1)./2;
    X=interp1(rpix,a,r_length);
else
```

asi_read_m6.m

This program is used to read all-sky data form file. It supports different file formats. The program also has the possibility to mask out areas outside a specified field-of-view.

This program was originally written by Espen Trondsen, and only some small changes has been done. The important ones is the support for header information in .keo files and support for .jpg files. This program uses a function imcircle.m written by John McCarthy.

```
function [data, varargout] = asi_read_m6(in_file, varargin)
%
% Read an AllSky Image file.
%
% Usage:
% asi_read(filename); or
% data = asi_read(filename); returns the image data matrix
% [data, varargout] = asi_read(filename, varargout) returns the data and a struct
% containing header information
% file_info
% time
% wavel
% filter_no
% ii_gain
% exp
% site
%
% inputvariables: 'fov', 'rot', 'size', 'mask', 'ud', 'uint16'
% The last three are single arguments, the others need a number after.
% Example:
% [data, head]=asi_read(filename, 'mask', 'fov', 75, 'size', [300 300]);


% TODO: linse-fov,
% tic/toc
%
```

```
% MN/GN
% pcolor/imagesc optim
% check for correct arguments,
% lyr_pmis, rot matr pmis/png,
% ekstrahere scan, egen output, annet fov enn bilde
%
% mer feilmeldinger

% .keo (herb) lagt inn. mangler file_info

% Reading of header information from .keo files and suport for .jpg files
% added by Njål

% ***** File reading and handling ******

%tic

% Check that no of in- and output arguments are within limits
error(nargchk(1, 10, nargin));
error(nargoutchk(0, 2, nargout));

% Split filename into parts for later use.
[fpath, fname, fext, fver] = fileparts(in_file);

% Read in_file into mtx and collect header info. Different handling for
% .png, .keo and PMIS format. .keo images are from Herb's 4" imager. Try/catch to give error
% message while problem to read or extract file (and file info)

if fext == '.png'
    try
        data = double(imread(in_file));
        head = imfinfo(in_file);

        file_info.time = datenum(str2num(fname(4:7)), str2num(fname(8:9)), str2num(fname
            (10:11)), ...
           str2num(fname(13:14)), str2num(fname(15:16)), str2num(fname(17:18)));
        file_info.wavel = fname(20:23);
        file_info.filter_no = str2num(head.Description(strfind(head.Description, '
            FILTER_NO')+10));
        file_info.ii_gain = str2num(head.Description(strfind(head.Description, 'II_G')+8)
            );
        file_info.exp = str2num(head.Description(strfind(head.Description, 'INTEGR')
            +(17:23)));
        file_info.site = lower(fname(1:3));

    catch
        error(['Can␣not␣open␣', in_file, '.␣Or␣at␣least␣in␣try-catch␣(open␣.png.']);
    end

elseif fext == '.jpg'
    try
        dd=imread(in_file);
        data = double(dd(:,:,1));
        head = imfinfo(in_file);

        file_info.time = datenum(str2num(['20' fname(1:2)]), str2num(fname(3:4)), str2num
            (fname(5:6)), ...
           str2num(fname(8:9)), str2num(fname(10:11)), str2num(fname(12:13)));
        file_info.wavel = fname(15:18);
```

```
        file_info.site = lower(fname(20:22));
        file_info.head=head;
    catch
        error(['Can␣not␣open␣', in_file, '.␣Or␣at␣least␣in␣try-catch␣(open␣.jpg.']);
    end

elseif fext == '.keo'
    fin = fopen(strcat(in_file),'r');


    % Generate error-message if file cannot be opened.
    if fin < 0
        error(['Can␣not␣open␣', in_file, '.']);
    end

    % Read image as little-endian, uint16, store as uint16 in 670x650 matrix
    data = double(fread(fin, [670 650], 'uint16=>uint16', 'l'));
    fclose(fin);
    % Reading header information; Njål
    head= data(1:20);
    file_info.time = datenum(head(1),head(2),head(3),head(4),head(5),head(6));
    file_info.wavel = head(7);
    %file_info.filter_no =
    file_info.ii_gain = head(8);
    file_info.exp = head(9)./10;
    file_info.lat=head(10)+head(11)./60+head(12)./3600;
    file_info.lon=360-(head(13)+head(14)./60+head(15)./3600);
    file_info.fovdeg=head(16);
    file_info.angle2=head(17);
    file_info.angle3=head(18);
    file_info.angle4=head(19);
    file_info.site = 'nya_am';
    file_info.head=head;

    if find(strcmp(varargin, 'calib_am'));
        load am_aver2;
        data=data./im2;
    end

else % file is supposed to be .pmis

    fin = fopen(in_file,'r','l');   % Open in_file, read-only, little-endian.
    if fin < 0 % Generate error-message if file cannot be opened.
        error(['Can␣not␣open␣', in_file, '.']);
    end

    fseek(fin, 61, 'bof');
    [head, le] = fscanf(fin, '%c', 50);

    file_info.time = datenum(str2num(head(1:4)), str2num(head(6:7)), str2num(head(9:10))
        , ...
        str2num(head(12:13)), str2num(head(15:16)), str2num(head(18:19)));

    % Find position of "keywords" in header
    W_idx = [strfind(head, 'W') strfind(head, 'F')];
    F_idx = [strfind(head, 'F') strfind(head, 'G')];
    G_idx = [strfind(head, 'G') strfind(head, 'E')];
    E_idx = [strfind(head, 'E') strfind(head, 'N')];
    S_idx = [strfind(head, 'S') strfind(head, 'L')];
```

```
    % Extract header info
    file_info.wavel = head(W_idx(1)+1:W_idx(2)-1);
    file_info.filter_no = str2num(head(F_idx(1)+1));
    file_info.ii_gain = str2num(head(G_idx(1)+1));
    file_info.exp = str2num(head(E_idx(1)+1:E_idx(2)-1));
    if length(S_idx)>1;
        file_info.site = lower(head(S_idx(1)+1:S_idx(2)-1));
    else
        file_info.site ='nya';
    end

    % Set position in in_file to beginning of image matrix.
    fseek(fin, 180, 'bof');

    % Read the image portion of in_file to matrix data. Close file
    data = fread(fin, [512 512], 'short');
    fclose(fin);
end

% Construct file name for loading site parameter info. LYR is divided in to
% parts due to two different file formats
if strcmp(file_info.site, 'lyr') && strcmp(fext, '.png')
    site_dta = strcat(file_info.site, '_info_png');
else
    site_dta = strcat(file_info.site, '_info_m6');
end
%Don't load site data for nya_am
%if ~strcmp(file_info.site, 'nya_am')
    load(site_dta);
    %end

% *** Additional image processing based on optional input arguments ***

if length(varargin) > 0

    % Defining/extracting choosen FoV from mtx
    if find(strcmp(varargin, 'fov'));%, 1) ------------------------
        fov_idx = find(strcmp(varargin, 'fov'));%, 1); ------------------------
        fov=varargin{fov_idx+1};
        fov_pix = floor(site_info.radius*fov/70);
        data=data(site_info.r_center-fov_pix:site_info.r_center+fov_pix, ...
            site_info.c_center-fov_pix:site_info.c_center+fov_pix);
    end

    % Rotate image according to input parameter
    if find(strcmp(varargin, 'rot'));%, 1)
        ------------------------------------
        rot_idx = find(strcmp(varargin, 'rot'));%, 1);
        rot = varargin{rot_idx+1};
        data = imrotate(data, rot, 'crop');
    end

    % Apply up/down mirroring
    if find(strcmp(varargin, 'ud'));%, 1)
        data=flipud(data);
    end

    % Apply mask around FoV. All pixels outside FoV cicle are set to NaN;
```

```
    if find(strcmp(varargin, 'mask'));%, 1)
        SP=imcircle(2*fov_pix+1);
        % Set all pixels outside FoV to NaN
        SP(find(SP==0))=NaN;
        data=data+SP;
    end

    % Convert mtx to uint16 instead of double. NaN's are set to 0!!!
    if find(strcmp(varargin, 'uint16'));%, 1)
        data = uint16(data);
    end

    % Setting size of output mtx. Size can be in percent of origin like 0.8
    % or 3.2 or exact size given as a rc vector e.g. [300 300]
    if find(strcmp(varargin, 'size'));%, 1)
        size_idx = find(strcmp(varargin, 'size'), 1);
        mtx_size = varargin{size_idx+1};
        data = imresize(data, mtx_size);
    end


end

% OBS tenk plassering! Rett etter fov? Disable uint16?
if find(strcmp(varargin, 'calib'));%, 1)

    % calibinfo må legges i site info

    % ff_ er forstavelse for flatfield
    ff_x = linspace(-fov,fov,size(data,1))%-fov:(140./358):fov;
    ff_y = ff_x;

    for i = 1:length(ff_x);
        for j = 1:length(ff_y);
            M(i,j) = sqrt(ff_x(i)^2 + ff_y(j)^2);
        end
    end

    %Binær maske
    msk = imcircle(length(ff_x));
    msk(find(msk==0)) = NaN;
    M = M.*msk;

    MM = -8.23.*10.^(-5).*M.^2 - 1.5.*10.^(-3).*M + 1;
    %size_dat=size(data);
    %MM = imresize(MM,size(data));
    data = data./MM.*8.618/file_info.exp;
end

% OBS tenk plassering! Rett etter calib? Disable uint16?

% ***** Assign output variables *****

if nargout == 1
    varargout = {};
elseif nargout == 2
    varargout = {file_info};
end
```

```
%toc
```

readMspData_hour_int

This program is a modified version of readMspData_day.m written by Espen Trondsen. The major change is the possibility to interpolate small time gaps int the data to create an even time axis.

```
function [n_keo, n_time] = readMspData_hour(day, varargin)
%plots limitet and calibrated keograms
%Interpolates the data along the timeaxis if the timeaxis is uneven.

% debug er en ekstra løkke for å enkelt kunne slå av og på
% debugginginformasjon når programmet kjører.
debug = 0;

if debug == 1
    tic
end

limits = [];
%limits_m = [];
time_vec = [];
ch_mtx = [];

%Setting time limits for the plot
xlimit= [datenum(0,0,0,17,0,0) datenum(0,0,0,24,0,0)];
%if nargin-1 == 0
run_aver = 1;
%else
% run_aver = varargin{1};
%end

wbar=waitbar(0, 'Reading␣MSP␣data␣files...');
for hour=17:23 %Hours in the plot
    waitbar((hour+1)/24);

    %Corrections for plot crossing midnight
    if hour >23
        hour = hour-24;
        d_vec = datevec(datenum(str2num(day(1:4)), str2num(day(5:6)),str2num(day(7:8)))
            +1);
        day = sprintf('%04u%02u%02u',d_vec(1:3));
    end
    try
        % Correct for files older than year 2000; Njål
        if str2num(num2str(day(1:4)))> 2000
            file=day;
        else
            file=num2str(day(3:8));
        end

        %Data directory and file name
        file = strcat('E:\data_nya\',...
            num2str(day(1:4)), '\', num2str(day(5:6)), '\n', file, '.', sprintf('%2.2i',
                hour), 'f');

        %Reads one hour of data
```

```
        [ch_mtx_hour, time_vec_hour, ChDirGPS, limits, status] = readMspHour_m6(file,'
            calib');


    catch
        if debug == 1
            disp(['Something␣wrong␣with␣hour:␣' num2str(hour)]);
        end
        %If data is empty
        ch_mtx_hour = ((1:181).*NaN)';
        for i =2:4
            ch_mtx_hour(:,:,i) = ((1:181).*NaN)';
        end
        time_vec_hour= datenum(str2num(day(1:4)),str2num(day(5:6)),str2num(day(7:8)),hour
            ,0,0);
    end

    %Concatonate data and timeaxis
    time_vec = cat(2, time_vec, time_vec_hour);
    ch_mtx = cat(2, ch_mtx, ch_mtx_hour);


    if debug ==1
        disp(strcat('OK␣hour', num2str(hour)));
    end

end
close(wbar);

%Remove zero data en edges
ch_mtx(find(ch_mtx==0))=NaN;
if str2num(day) < 20010000 & length(limits)>0
    if limits(:,1)> [0; 0]
        ch_mtx(1:limits(1,:),:,:)=NaN;
        ch_mtx(limits(2,:):size(ch_mtx,1),:,:)=NaN;
    end
end
% ************************************************************************

%Interpolation borders
start = 15;
stop = 23;

%Remove date information from timeaxis
time_vec=time_vec-datenum(str2num(day(1:4)),str2num(day(5:6)),str2num(day(7:8)));

%Create evenly spaced time axis for the interpolated data.
n_time=linspace(datenum(0, 0, 0, start, 0, 0), datenum(0, 0, 0, stop, 60, 00), (stop-
    start+1).*224);%164);

%Interpolate along timeaxis to create evenly spaced data
try
for ch = 1:4
    n_keo(:,:,ch) = interp1(time_vec,ch_mtx(:,:,ch)',n_time)';
end
catch
    n_keo = 0;
    n_time= 0
    break;
```

```
end

%Localize OCB usind a fit to a step function (Ignoring the edges)
%[OCB val]=find_OCB(n_keo(:,:,1)); %Not in use

%Setting color axis limits for the plot
climits=[2.5 4;2.2 4.5; 1.5 3.5;1.5 3]


fig = figure('Position', [50 50 950 700], 'PaperPositionMode', 'auto');
for ch=1:4
    subplot(4,1,ch);
    pcolor(n_time,1:181, flipud(log10(n_keo(:,:,ch).*1000))), shading flat,colormap(jet
        (256)),...
        caxis(climits(ch,:)),...%
        datetick, colorbar;xlim(xlimit);
    set(gca, 'TickDir', 'out');
    set(gca,'YTick',0:30:180 )
    set(gca,'YTickLabel',180:-30:0);
    switch ch
        case 1
            ylabel('630.0 nm');
            %Plotting OCB (Not in use)
            %hold on; plot(n_time,181-OCB,'k','linewidth',1);

        case 2
            ylabel('557.7 nm');
        case 3
            ylabel('427.8 nm');
        case 4
            ylabel('486.1 nm');
    end
end

if debug == 1
    toc
end
dato=datenum(str2num(day(1:4)),str2num(day(5:6)),str2num(day(7:8)));
[ax, h1] = suplabel(['Ny-Ålesund MSP, ' datestr(dato)], 't');
set(h1, 'FontSize', 18);

[ax, h2] = suplabel('Intensities in log(R)', 'x');
set(h2, 'FontSize', 12);

save_name = strcat('.\all\details\NYA_MSP_', datestr(dato, 29));

%print('-dpng', '-r0', save_name);
%clf;
%close(fig);
```

readMspHour_m6

This is a program that reads one hour data from the MSP. It is written by Espen Trondsen and the only change done to it is adding some extra calibration data. (The code is not included here.)

median5x

This is a 5×5 median filter.

```
function img_out = median5x(img_in);

s = size(img_in);
img_out = ones(s(1),s(2)).*NaN;
for j= 3:s(2)-2
    for i = 3:s(1)-2
        img_out(i,j)=median(reshape(img_in (i-2:i+2,j-2:j+2),25,1));
    end
end
```

find_OCB

A program that locates the Open-closed field line boundary (OCB) in MSP data using an algorithm described by Blanchard et al. (1995). The program tries to find the best fit of the data to a step function in latitude. It also uses some criteria to check if the OCB is found (see section 4.2.2 on page 27).

```
function [out,val]=find_OCB(in)


Ip = in;
Ia = in;

%Calculate polar cap and auroral intensities
for i = 1:size(in,1)
    Ip(i,:)= nanmean(in(1:i,:));
    Ia(i,:)= nanmean(in(i:size(in,1),:));
end

fit = zeros(size(in));
step_f = zeros(size(in));

%Find best fit to a step function
for i= 1:size(in,1)
    step_f(1:i-1,:)=repmat(Ip(i,:),i-1,1);
    step_f(i,:) =(Ip(i,:)+Ia(i,:))./2;
    step_f(i+1:size(step_f,1),:)= repmat(Ia(i,:),size(step_f,1)-i,1);
    fit(i,:) = nansum((in-step_f).^2);
end
[C out] = min(fit);

for i=1:size(in,2)
    val(i) = in(out(i),i);
end


step_f = zeros(1,size(in,1));
for i= 1:size(in,2)
    % Polar cap intensity less than 1KR, 300R
    k1(i) = Ip(out(i),i) < 1.5;

    % The step increase in intensity is more than 75% of polar cap
    % intensity
    k2(i) =(Ia(out(i),i)-Ip(out(i),i))./Ip(out(i),i) > 0.75;
```

```
    %Construct the step function
    step_f(1:out(i)-1)=Ip(out(i),i);
    step_f(out(i)) =(Ip(out(i),i)+Ia(out(i),i))./2;
    step_f((out(i)+1):length(step_f))= Ia(out(i),i);

    %calculate corolation
    sx =sqrt(nanmean(step_f.^2)-(nanmean(step_f)).^2);
    sy =sqrt(nanmean(in(:,i).^2)-(nanmean(in(:,i))).^2);
    sxy = nanmean(step_f'.*in(:,i))-nanmean(step_f).*nanmean(in(:,i));
    rxy(i) = sxy./(sx.*sy);

    %Find where polar cap intensities is larger than auroral intensities
    k4(i) = Ip(out(i),i) < Ia(out(i),i);
end

%Check if corolation exceeds 80%
k3=rxy>0.8;

%Remove data where less than two criterias is satisfied
out(find(k1+k2+k3 < 2 ))=NaN;

% Remove date where polar cap intensities is larger than auroral
% intensities
out(find(k4 < 0 ))=NaN;
```

Bibliography

Baker, K. B. and Wing, S.: A new magnetic coordinate system for conjugate studies at high latitudes, Journal of Geophysical Research, 94, 9139–9143, 1989.

Blanchard, G. T., Lyons, L. R., Samson, J. C., and Rich, F. J.: Locating the polar cap boundary from observations of 6300 A auroral emission, Journal of Geophysical Research, 100, 7855–7862, 1995.

Brekke, A.: Physics of the upper polar atmosphere, Wiley-Praxis series in atmospheric physics, Wiley, 1997.

Carlson, Jr., H. C.: Dark polar ionosphere: Progress and future challenges, Radio Science, 29, 157–165, 1994.

Coley, W. R. and Heelis, R. A.: Structure and occurrence of polar ionization patches, Journal of Geophysical Research, 103, 2201–2208, doi:10.1029/97JA03345, 1998.

Cowley, S. W. H.: Magnetospheric asymmetries associated with the y-component of the IMF, Planetary and Space Science, 29, 79–96, doi:10.1016/0032-0633(81)90141-0, 1981.

Cowley, S. W. H. and Lockwood, M.: Excitation and decay of solar wind-driven flows in the magnetosphere-ionosphere system, Annales Geophysicae, 10, 103 – 115, 1992.

Crowley, G.: Critical review of ionospheric patches and blobs, URSI Review of Radio Sci. 1993 – 1996, pp. 619 – 648, 1996.

Dungey, J. W.: Interplanetary Magnetic Field and the Auroral Zones, Physical Review Letters, 6, 47–48, doi:10.1103/PhysRevLett.6.47, 1961.

Dyrland, M. E.: A multi-instrument analysis of postnoon auroral morphology and lobe reconnection events during southeast IMF orientation, Master's thesis, University of Oslo, 2005.

Foster, J. C., Coster, A. J., Erickson, P. J., Holt, J. M., Lind, F. D., Rideout, W., McCready, M., van Eyken, A., Barnes, R. J., Greenwald, R. A., and Rich, F. J.: Multiradar observations of the polar tongue of ionization, Journal of Geophysical Research (Space Physics), 110, 9–+, doi:10.1029/2004JA010928, 2005.

Garrard, T. L., Davis, A. J., Hammond, J. S., and Sears, S. R.: The ACE Science Center, Space Science Reviews, 86, 649–663, doi:10.1023/A:1005096317576, 1998.

Hosokawa, K., Shiokawa, K., Otsuka, Y., Nakajima, A., Ogawa, T., and Kelly, J. D.: Estimating drift velocity of polar cap patches with all-sky airglow imager at Resolute Bay, Canada, Geophysical Research Letters, 33, 15 111–+, doi:10.1029/2006GL026916, 2006.

KEO Consultants: Telecentric lens systems for wide-field low-f# monochromatic imaging, Tech. rep., KEO Consultants, 1993.

KEO Consultants: All-sky Imaging System for University of Oslo, Tech. rep., KEO Consultants, 1995.

Khan, H. and Cowley, S. W. H.: Observations of the response time of high-latitude ionospheric convection to variations in the interplanetary magnetic field using EISCAT and IMP-8 data, Annales Geophysicae, 17, 1306–1335, 1999.

Kivelson, M. G. and Russel, C. T., eds.: Introduction to space physics, The press syndicate of the University of Cambridge, 1995.

Lorentzen, D. A., Shumilov, N., and Moen, J.: Drifting airglow patches in relation to tail reconnection, Geophysical reasearche letters, 31, 2806–+, doi:10.1029/2003GL017785, 2004.

Lyons, L. R., Nagai, T., Blanchard, G. T., Samson, J. C., Yamamoto, T., Mukai, T., Nishida, A., and Kokobun, S.: Association between Geotail plasma flows and auroral poleward boundary intensifications observed by CANOPUS photometers, Journal of Geophysical Research, 104, 4485–4500, doi:10.1029/1998JA900140, 1999.

McComas, D. J., Bame, S. J., Barker, P., Feldman, W. C., Phillips, J. L., Riley, P., and Griffee, J. W.: Solar Wind Electron Proton Alpha Monitor (SWEPAM) for the Advanced Composition Explorer, Space Science Reviews, 86, 563–612, doi:10.1023/A:1005040232597, 1998.

Newell, P. T., Ruohoniemi, J. M., and Meng, C.-I.: Maps of precipitation by source region, binned by IMF, with inertial convection streamlines, Journal of Geophysical Research (Space Physics), 109, 10 206–+, doi:10.1029/2004JA010499, 2004.

Paschmann, G.: Geomagnetism, vol. 4, chap. 3 "The Earth's Magnetopause", pp. 302 – 307, Academic Press Limited, 1991.

Pécseli, H. L.: Selected topics in plasma physics, 2005.

Raj, A., Phan, T., Lin, R. P., and Angelopoulos, V.: Wind survey of high-speed bulk flows and field-aligned beams in the near-Earth plasma sheet, Journal of Geophysical Research (Space Physics), 107, 3–1, doi:10.1029/2001JA007547, 2002.

Ridley, A. J.: Estimations of the uncertainty in timing the relationship between magnetospheric and solar wind processes, Journal of Atmospheric and Terrestrial Physics, 62, 757–771, 2000.

Ridley, A. J., Lu, G., Clauer, C. R., and Papitashvili, V. O.: A statistical study of the ionospheric convection response to changing interplanetary magnetic field conditions using the assimilative mapping of ionospheric electrodynamics technique, Journal of Geophysical Research, 103, 4023–4040, doi:10.1029/97JA03328, 1998.

Rodger, A. S., Pinnock, M., Dudeney, J. R., and Baker, K. B.: A new mechanism for polar patch formation, Journal of Geophysical Research, 99, 6425–6436, 1994.

Ruohoniemi, J. M. and Baker, K. B.: Large-scale imaging of high-latitude convection with Super Dual Auroral Radar Network HF radar observations, Journal of Geophysical Research, 103, 20 797–20 811, doi:10.1029/98JA01288, 1998.

Ruohoniemi, J. M. and Greenwald, R. A.: Statistical patterns of high-latitude convection obtained from Goose Bay HF radar observations, Journal of Geophysical Research, 101, 21 743–21 764, doi:10.1029/96JA01584, 1996.

Ruohoniemi, J. M. and Greenwald, R. A.: Dependencies of high-latitude plasma convection: Consideration of interplanetary magnetic field, seasonal, and universal time factors in statistical patterns, Journal of Geophysical Research (Space Physics), 110, 9204–+, doi:10.1029/2004JA010815, 2005.

Sandholt, P. E., Carlson, H. C., and Egeland, A.: Dayside and Polar Cap Aurora, vol. 270 of *Astrophysics and Space Science Library*, Kluwer Academic Publisher, 2002.

Shue, J.-H., Song, P., Russell, C. T., Steinberg, J. T., Chao, J. K., Zastenker, G., Vaisberg, O. L., Kokubun, S., Singer, H. J., Detman, T. R., and Kawano, H.: Magnetopause location under extreme solar wind conditions, Journal of Geophysical Research, 103, 17 691–17 700, doi:10.1029/98JA01103, 1998.

Smith, C. W., L'Heureux, J., Ness, N. F., Acuña, M. H., Burlaga, L. F., and Scheifele, J.: The ACE Magnetic Fields Experiment, Space Science Reviews, 86, 613–632, doi:10.1023/A:1005092216668, 1998.

Sojka, J. J., Bowline, M. D., Schunk, R. W., Decker, D. T., Valladares, C. E., Sheehan, R., Anderson, D. N., and Heelis, R. A.: Modeling polar cap F-region patches using time varying convection, Geophysical Research Letters, 20, 1783–1786, 1993.

Sojka, J. J., Bowline, M. D., and Schunk, R. W.: Patches in the polar ionosphere: UT and seasonal dependence, Journal of Geophysical Research, 99, 14 959–14 970, doi:10.1029/93JA03327, 1994.

Stone, E. C., Frandsen, A. M., Mewaldt, R. A., Christian, E. R., Margolies, D., Ormes, J. F., and Snow, F.: The Advanced Composition Explorer, Space Science Reviews, 86, 1–22, doi:10.1023/A:1005082526237, 1998.

Weimer, D. R.: Models of high-latitude electric potentials derived with a least error fit of spherical harmonic coefficients, Journal of Geophysical Research, 100, 19 595–19 608, doi:10.1029/95JA01755, 1995.

URL's

ACE mission website: `http://www.srl.caltech.edu/ACE/`.

KEO Scientific Ltd.: `http://keoscientific.com/`.

NASA/Goddard Space Flight Center, ModelWeb: `http://modelweb.gsfc.nasa.gov/models/cgm/cgm.html`.

SuperDARN - Super Dual Auroral Radar Network: `http://superdarn.jhuapl.edu/`.